Circadian rhythm orthologs drive pulses of heterochronic miRNA transcription in *C. elegans*

Brian Kinney[1]*, Shubham Sahu[2]*, Natalia Stec[1], Kelly Hills-Muckey[1], Dexter W. Adams[3,4], Jing Wang[1], Matt Jaremako[3], Leemor Joshua-Tor[3], Wolfgang Keil[2,†] , Christopher M. Hammell[1,†]

[1]Cold Spring Harbor Laboratory, Cold Spring Harbor, NY 11724, USA.

[2]Institut Curie, Université PSL, Sorbonne Université, CNRS UMR168 Laboratoire Physico Chimie Curie, 75005 Paris, France.

[3]Howard Hughes Medical Institute, W. M. Keck Structural Biology Laboratory, Cold Spring Harbor Laboratory, Cold Spring Harbor, NY, 11724, USA

[4]Graduate Program in Genetics, Stony Brook University; Stony Brook, NY 11794, USA

*These authors contributed equally

[†]Correspondence: wolfgang.keil@curie.fr (W.K.); chammell@cshl.edu (C.M.H.) (lead contact)

Abstract: The *C. elegans* transcriptome exhibits reproducible, periodic patterns that are phase-locked with features of the larval molting cycle, but the gene regulatory networks underlying this interdependency are unknown. We show here that repeated transcriptional pulses of the *lin-4* temporal patterning miRNA are generated by cooperative binding between the *C. elegans* orthologs of master circadian regulators Rev-Erb and ROR to elements upstream of the *lin-4* gene. Remarkably, the precise timing and length of *lin-4* transcriptional pulses are dictated by the phased overlap of NHR-85$^{\text{Rev-Erb}}$ and NHR-23^{ROR} temporal expression patterns. We also demonstrate that LIN-42^{Period} functions in a similar capacity to its circadian orthologs to negatively regulate periodic transcription but does so by limiting the duration of NHR-85$^{\text{Rev-Erb}}$/NHR-23^{ROR} cooperative activity at the *lin-4* gene.

Summary: Orthologs of circadian clock genes generate repeated transcriptional pulses of developmental timing genes in *C. elegans*

35 Ontogenesis is an inherently dynamic process during which the timing and sequence of
36 developmental events must be organized through coordinated patterns of gene expression. The four
37 larval stages of *C. elegans* are characterized by stage-specific patterns of cell division, cell
38 differentiation, and cuticle formation that occur during intermolt periods (*1*). Classical forward genetic
39 approaches have identified several highly conserved temporal selector genes that combinatorially
40 program stage-specific patterns of cell fate specification during post-embryonic development (*2*).
41 Transitions through successive stage-specific developmental cell fate programs are mediated by the
42 accumulation of several microRNAs (miRNAs) that post-transcriptionally regulate the expression of
43 their temporal selector gene targets (*3*). Importantly, the activity of these regulatory RNAs within this
44 so-called heterochronic gene regulatory network (GRN) is dosage sensitive, meaning that abnormally
45 lower or higher dosages of heterochronic miRNAs result in wholesale skipping or reiteration of
46 discrete stage-specific developmental programs (*3-7*). The sequential expression of heterochronic
47 miRNAs therefore couple temporal cell-fate progression to the repetitive larval molting cycles.

48 Approximately 20% of the *C. elegans* transcriptome exhibits reproducible, periodic expression
49 patterns that are phase-locked with features of the molting cycle (*8-11*). These patterns and their
50 coordination are genetically controlled, occur with exquisite robustness regardless of environmental
51 and physiological stresses, and are independent of life-history (*8-11*) suggesting that a system
52 patterns gene expression to orchestrate the temporal coordination of developmental processes.
53 Remarkably, the transcription of heterochronic miRNAs is also coupled to the larval molting cycles
54 (*6, 7, 10, 12*). While several transcription factors (TFs) have been implicated in controlling
55 heterochronic miRNA transcription (*13-18*), we lack mechanistic understanding of how miRNA gene
56 expression is coupled to the molting clock, and how the precise transcriptional dynamics of microRNA
57 loci - including pulse amplitude, duration, and phase of expression within each cycle - is controlled to
58 tightly govern the critical dynamics of miRNA dosage as development progresses.

59

60 **Pulsatile transcription of *lin-4* is coordinated with larval stage progression**

61 Within the heterochronic GRN, the *lin-4* gene encodes a miRNA that controls the transition
62 from L1- to L2-stage patterns of gene expression (*19*) and is expressed periodically throughout all
63 larval stages (*11*). To directly measure *lin-4* transcriptional kinetics, we implemented the MS2/MCP-
64 GFP tethering system, which exploits the natural affinity between RNA loops derived from MS2
65 bacteriophage and a co-expressed MS2 coat protein fused to green fluorescent protein (MCP-
66 GFP)(*20*). By genetically encoding the MS2 hairpins within a gene of interest, nascent RNAs can be
67 directly imaged in living cells through their ability concentrate MCP-GFP at the sites of RNA synthesis

68 (Fig. 1A). To visualize *lin-4* transcription, we generated a ~4kb transgene harboring the *lin-4* precursor
69 RNA followed by 24 copies of a synthetic MS2 hairpin upstream of the polyadenylation sequences
70 and the upstream regulatory information required to drive normal *lin-4* transcription (*11*) (fig. S1A)(*21*).
71 This transgene fully rescues the developmental phenotypes associated with the *lin-4* null allele (*lin-*
72 *4(e912))* (fig. S1). We also drove ubiquitous expression of MCP fused to GFP (MCP-GFP) to detect
73 MS2-tagged RNAs, and a histone H2B subunit (HIS-58) fused to mCherry to locate nuclei (fig. S1A).
74 Examination of L3-staged transgenic animals revealed that dynamic *lin-4* expression (MCP-GFP foci)
75 occurred from each *lin-4::MS2* locus in somatic tissue types known to transcribe *lin-4* (Fig. 1B). MCP-
76 GFP foci were never observed in developing embryos (n > 50) or in starvation arrested L1 larva (n =
77 23); consistent with the activation of *lin-4* transcription after the initiation of larval development (*4*).

78 Next, we used our microfluidics platform to perform live spinning-disk confocal microscopy of
79 developing *C. elegans* larvae harboring *lin-4::24xMS2/MCP-GFP* system (*11, 22*). We focused on
80 quantifying expression dynamics in hypodermal cells (seam, hyp7 and vulval precursor cells (VPCs))
81 where the timing of transcriptional activity within a given larval stage can be accurately assessed in
82 relation to the occurrence of precisely timed stage-specific cell division patterns (*1*). We first screened
83 for periods of *lin-4* transcriptional activity by imaging at 15min time intervals from early first larval
84 stage (L1) to mid L4 stages (~60h) (n>10). This revealed that *lin-4::24xMS2* transcription was highly
85 pulsatile, with a single transcriptional episode of ~45-90min in each cell during each larval stage,
86 followed by extremely long periods of inactivity (>8hrs at 20°C) (Fig. 1C). Transcriptional activation
87 across cells within the entire hypodermis was highly concordant, exhibiting similar transcriptional on
88 and off times for all *lin-4::24xMS2* loci (Fig. 1E). For instance, during the mid-L3 stage, the
89 appearance of *lin-4::24xMS2* expression throughout the hypodermis generally occurred within
90 minutes of the first VPC divisions (P3.p or P4.p) and were completed by the divisions of P5.p-P7.p (n
91 = 15) (Fig. 1C).

92 Based on these observations, we performed short-term imaging time courses (<6h) at 4min
93 intervals in staged larvae to capture transcriptional epochs at high temporal resolution. During
94 transcriptional episodes, we detected near synchronous accumulation of MCP-GFP foci at each
95 hypodermal *lin-4::24xMS2* locus for 60-90 minutes (Fig. 1D-E, Suppl. Movie 1,2) (>15 animals). We
96 found no signs of "bursty" transcription (*23*) as loci generally stayed on for the entire transcriptional
97 episode (Suppl. Movie 1,2). These features were independent of the number of *lin-4::24xMS2* loci
98 per nucleus as cell types that undergo endoreduplication (i.e., hyp7 cells) exhibited MCP-GFP foci
99 dynamics indistinguishable from diploid cells (Fig. 1D). The dynamic features of *lin-4::24xMS2*
100 expression in hypodermal cells were similar across different developmental stages (Fig. 1E)

101 suggesting that the same regulatory programs controlling *lin-4* transcription were repeated at each
102 larval stage. Finally, the pulsatile nature of transcriptional activation occurred in a broad array of
103 additional cell types that normally express *lin-4*. These include pharyngeal muscles and intestinal
104 cells in which the phase of transcriptional induction is shifted later compared to patterns observed in
105 hypodermal cells and the duration of pulses are extended (fig. S2).

106

107 **NHR-85$^{Rev\text{-}Erb}$ and NHR-23^{ROR} interact with the regulatory regions that control repetitive *lin-4***
108 **transcription**

109 We previously demonstrated that highly pulsatile transcription from the *lin-4* locus is
110 dependent on the upstream *lin-4* PCE (*p*ulse *c*ontrol *e*lement) (*11*). To identify candidate TFs that
111 bind this conserved regulatory sequence, we performed a yeast-one-hybrid screen using the entire
112 514bp *lin-4* PCE as bait and identified three TFs (BLMP-1, NHR-23 and NHR-85) (Fig. 2A). BLMP-1
113 controls the amplitude of *lin-4* expression and functions as a pioneer factor to decompact the *lin-4*
114 locus throughout development (*11*). *nhr-85* and *nhr-23* encode two nuclear hormone receptors
115 (NHRs) that are the closest nematode orthologs of human circadian TFs Rev-Erb and ROR,
116 respectively (Fig. 2B). Analysis of publicly available ChIP-seq data indicated that all three proteins
117 interact *in vivo* with *lin-4* regulatory sequences, which contain putative consensus binding sites for
118 each TF (Fig. 2A). Furthermore, NHR-85$^{Rev\text{-}Erb}$, NHR-23^{ROR} and BLMP-1 binding sites are highly
119 overlapping and enriched in the promoters of numerous cyclically expressed protein coding genes
120 and heterochronic miRNAs (fig. S3) (table S1 and S2).

121 **NHR-85$^{Rev\text{-}Erb}$ and NHR-23^{ROR} heterodimerize and bind cooperatively *lin-4* regulatory elements**

122 Nuclear hormone receptors often bind cooperatively as homo- or hetero-dimeric complexes
123 at closely spaced cis-regulatory DNA elements (*24-26*). Several features of NHR-85$^{Rev\text{-}Erb}$, NHR-23^{ROR}
124 and the *lin-4* PCE suggest that this may also be the case for *lin-4* transcription. First, NHR-85$^{Rev\text{-}Erb}$
125 and NHR-23^{ROR} share significant sequence homology within their ZnF C4-type DNA-binding domains
126 implicated in DNA interactions and dimerization, suggesting they may function at similar binding sites
127 (Fig. 2C)(*27*). Second, we found that NHR-85$^{Rev\text{-}Erb}$ and NHR-23^{ROR} could bind to form heterodimers
128 in yeast two-hybrid assays, which could be reconstituted *in vitro* with a binding affinity of 5.8 +/- 2.2
129 nM K_D (Fig. 2D,E). Third, sequences within the PCE element contain direct repeats of a GGTCA that
130 are contained in predicted binding sites of NHR-85$^{Rev\text{-}Erb}$ and NHR-23^{ROR} (Fig. 2F and G). Fourth, while
131 NHR-23^{ROR} alone could bind a DNA fragment at high TF/DNA molar ratios (fig. S4A,B), we found that

132 DNA binding assays containing concentrations of NHR-23^{ROR} that are insufficient to bind the PCE
133 alone are dramatically stimulated by the addition of NHR-85$^{Rev\text{-}Erb}$ (Fig. 2H,I). NHR-85$^{Rev\text{-}Erb}$ alone was
134 unable to reproducibly bind any *lin-4* PCE DNA fragments (fig. S4C). Finally, the cooperative binding
135 of NHR-85$^{Rev\text{-}Erb}$ and NHR-23^{ROR} to *lin-4* enhancer fragments requires the presence of both conserved
136 GGTCA direct repeats, suggesting these NHRs bind closely spaced regulatory elements as a
137 heterodimer (Fig. 2H).

138

139 **NHR-85$^{Rev\text{-}Erb}$, NHR-23^{ROR}, and LIN-42^{Period} expression is phased during each larval stage**

140 Previous studies indicate that LIN-42^{Period}, the *C. elegans* ortholog of the circadian Period
141 protein, negatively regulates the expression of *lin-4* throughout post-embryonic development (*7, 12,*
142 *28*). Given the roles of mammalian Period, ROR, Rev-Erb in controlling circadian gene regulation in
143 mouse and human, we examined potential regulatory relationships between the *C. elegans* orthologs
144 of these genes in the context of *lin-4* transcription. Single-cell expression analysis indicates that *nhr-*
145 *85* and *nhr-23* mRNAs are enriched in hypodermal and glial cells while *lin-42* is broadly expressed
146 (Fig. 3A)(*29*). *nhr-85* transcription initiates from an L1-stage arrest with a pulse of transcription that is
147 followed by a monotonic expression pattern at subsequent larval stages (Fig. 3B). In contrast, *nhr-23*
148 and *lin-42* mRNAs exhibit phased, high-amplitude oscillatory patterns of expression (Fig. 3B).

149 We next explored the temporal dynamics of NHR-85$^{Rev\text{-}Erb}$, NHR-23^{ROR} and LIN-42^{Period} protein
150 by quantifying the expression of endogenously-tagged alleles of each gene during the L4 stage, in
151 which the evenly-spaced, stereotyped morphological changes in vulval morphogenesis can be
152 directly correlated with developmental age (*30*). Consistent with previous characterization of NHR-
153 23^{ROR} and LIN-42^{Period} expression patterns determined using reporter transgenes (*31, 32*), each of
154 our endogenous reporters was expressed dynamically in hypodermal cells with a single peak of
155 expression that roughly matches the phased expression of their mRNAs (Fig. 3C). In contrast to the
156 flat expression of *nhr-85* transcripts in L2-L4 stages of development, we found that NHR-85$^{Rev\text{-}}$
157 ^{Erb}::GFP expression was highly dynamic, indicating substantial post-transcriptional regulation of NHR-
158 85$^{Rev\text{-}Erb}$ expression. Specifically, peak expression of NHR-85$^{Rev\text{-}Erb}$::GFP occurs at ecdysis (shortly
159 before NHR-23^{ROR}::mScarlet onset), becomes undetectable by the L4.3 stage of development, and
160 resumes at the L4.6 stage in an antiphasic manner to the expression pattern of LIN-42^{Period}::YFP (Fig.
161 3C). Highly similar phased expression patterns of these proteins are also maintained in L4-staged
162 vulval tissues (Fig. 3D) as well as in L3-staged hypodermal cells and VPCs (Fig. 4).

163

164 **The temporal overlap in NHR-85$^{Rev\text{-}Erb}$ and NHR-23^{ROR} expression correlates with *lin-4***
165 **transcriptional pulses**

166 The overlap in NHR-85$^{Rev\text{-}Erb}$::GFP and NHR-23^{ROR}::mScarlet expression during the L4 stage
167 lasts 60-90min (L4.2-L4.3) (Fig. 3D), the approximate duration of *lin-4* transcription in hypodermal
168 cells and VPCs at this same stage (Fig. 1D,E)(*30*). To compare the timing of these events, we
169 examined MCP-GFP localization in vulval cells during the L3 stage, where the rapid, stereotyped
170 vulval cell division patterns (*22*) enable precise determination of the timing of *lin-4::24xMS2*
171 transcription and TF dynamics. We found a striking correspondence between NHR-85$^{Rev\text{-}Erb}$ and
172 NHR-23^{ROR} co-expression and *lin-4::24xMS2* transcription (Fig. 4). Specifically, while the expression
173 of both nuclear receptors is phased, the transient expression of the *lin-4::24xMS2* transgene only
174 occurs during the brief period when both NHR proteins are expressed in VPCs (Fig. 4A). This almost
175 perfect correspondence is also maintained in hypodermal cells during this transcriptional cycle where
176 both NHR-85$^{Rev\text{-}Erb}$ expression and MCP-GFP foci are diminished near the completion of the first
177 round of VPC divisions (Fig. 1E and 3D). Importantly, the timing of NHR-85$^{Rev\text{-}Erb}$ downregulation is
178 also concurrent with onset of LIN-42^{Period} expression in VPCs and hypodermal cells (Fig. 3D and 4A).
179 The phased expression patterns of all TFs and the dynamics of MCP-GFP foci accumulation are also
180 conserved in the L4 stage of development (Fig. 4B). This indicates that the timing and duration of *lin-*
181 *4* transcriptional pulses are likely encoded by the dynamic expression patterns of these TFs (Fig. 4C).

182

183 **LIN-42^{Period} regulates NHR-85$^{Rev\text{-}Erb}$ levels to modulate the amplitude and duration of *lin-4***
184 **transcription**

185 Mutations in *lin-42^{Period}* produce late temporal patterning defects including precocious
186 expression of adult-specific genes in the L4 stage (Fig. 5A) (*6, 7, 33*). Mammalian Period orthologs
187 have been shown to interact with multiple NHRs and modulate their transcriptional activity (*34*). To
188 determine if LIN-42^{Period} could physically interact with other *C. elegans* NHRs, we systematically
189 probed LIN-42^{Period} interactions with a majority of the of *C. elegans* NHRs (243 of 284) using two-
190 hybrid assays. We identified 66 *C. elegans* NHRs that could interact with LIN-42^{Period} in yeast (fig.
191 S5A,B), including orthologs of Rev-Erb(NHR-85)(Fig. 5B), HNF4a(NHR-14, NHR-69) and
192 PPARα(NHR-119), indicating evolutionary conservation of physical interactions between *Period*
193 orthologs and related NHRs (Fig. S5A-B)(*34*). We mapped the domains of LIN-42^{Period} that are
194 required for NHR-85$^{Rev\text{-}Erb}$ binding and found that a minimal 51aa fragment present in both major LIN-
195 42^{Period} isoforms is sufficient to mediate interactions (Fig. 5A). This domain is distinct from the

196 interaction motifs implicated in mammalian Per2 and Rev-Erb (*34*). Neither LIN-42^{Period} isoform
197 interacts with NHR-23^{ROR} in two-hybrid assays (Fig. 5A).

198 Given the physical interaction between NHR-85$^{Rev\text{-}Erb}$ and LIN-42^{Period}, we asked whether
199 NHR-85$^{Rev\text{-}Erb}$ expression was required for the precocious phenotypes seen in *lin-42(lf)* mutants (*lin-*
200 *42(n1089)*). We found that *lin-42(lf)* heterochronic phenotypes are partially ameliorated by removing
201 *nhr-85* function. Specifically, precocious expression of *col-19::GFP* in both seam and hyp7 cells
202 observed in *lin-42(lf)* mutants is suppressed by *nhr-85* deletion; leaving weak expression in seam
203 cells in double mutants, while precocious deposition of adult alae was not suppressed (Fig. 5A). To
204 examine whether LIN-42^{Period} regulates NHR-85$^{Rev\text{-}Erb}$ temporal dynamics, we compared the dynamics
205 of NHR-85$^{Rev\text{-}Erb}$::GFP (and NHR-23^{ROR}::mScarlet) expression in wild-type and *lin-42(lf)* mutants. We
206 found that the expression of NHR-85$^{Rev\text{-}Erb}$ is altered in two ways by a *lin-42(lf)* mutation: First,
207 expression of NHR-85$^{Rev\text{-}Erb}$::GFP is ~2.3x more abundant at the beginning of the L4 stage in *lin-42*
208 mutants when compared to wild-type animals (Fig. 5C and D). Importantly, the periodic dampening
209 of NHR-85$^{Rev\text{-}Erb}$ expression at the L4.2 stage observed in wild-type animals (Fig. 3C,D) is altered in
210 *lin-42(lf)* mutants and NHR-85$^{Rev\text{-}Erb}$::GFP expression perdures into the L4.4 stage (Fig. 5C,D).
211 Mutations in *lin-42* do not alter the onset or duration of NHR-23^{ROR}::mScarlet accumulation in
212 hypodermal or vulval cells.

213 Our results suggest that timing of *lin-4* transcriptional pulses is defined by the brief co-
214 expression of NHR-85$^{Rev\text{-}Erb}$ and NHR-23^{ROR} (Fig. 4C). We hypothesized that the corresponding
215 increase in *lin-4* expression levels previously observed in *lin-42(lf)* mutants (*6, 7*) likely result from
216 alterations in *lin-4* transcription associated with mis-regulation of NHR-85$^{Rev\text{-}Erb}$ expression. To test
217 this, we examined expression of MCP-GFP foci throughout the L3 stage and found that, while a
218 majority of wild-type seam cells fire a single time (76%; 66 foci), the percentage of seam cells that
219 exhibit detectable *lin-4* transcription is dramatically increased in *lin-42* mutants (100%; 58 foci). This
220 indicates that *lin-42* normally dampens *lin-4* transcriptional pulses in wild-type animals. In addition to
221 elevating the likelihood *lin-4::24xMS2* transcription is above a threshold sufficient to generate
222 measurable MCP-GFP foci, *lin-42(lf)* mutations lead to an increase in the intensity of MCP-GFP foci
223 indicting that LIN-42^{Period} normally also limits Pol II loading at the *lin-4* locus (Fig. 5E). Time course
224 experiments revealed that overall duration of detectable transcription in seam cells is ~2.2 times
225 longer in *lin-42* mutants compared to wild-type (Fig. 5E). Consistent with our hypothesis that the
226 duration of *lin-4* transcription is dependent on the duration of NHR-85$^{Rev\text{-}Erb}$ expression, transcriptional
227 onset of *lin-4* occurs earlier in *lin-42* mutants and inappropriately extends through both the first and
228 second Pn.p divisions (Fig. 5F).

229 While *nhr-85(0)* mutants do not miss-express *col-19::GFP* (Fig. 5A), high-resolution imaging
230 experiments monitoring VPC divisions and *lin-4::24xMS2* expression indicate that two features of
231 developmental timing are altered in *nhr-85(0)* mutants. Transcriptional pulses of *lin-4::24xMS2* are
232 both robust and concordant in adjacent wild-type VPCs (Fig. 5G). In contrast, MCP-GFP foci in *nhr-*
233 *85(0)* mutants begin to accumulate at the same relative phase of L3-stage VPC development but are
234 dimmer and only transiently observed (Fig. 5G). Second, under isogenic imaging conditions, the rapid
235 and highly coordinated VPC divisions observed in wild-type animals is altered in *nhr-85(0)* mutants
236 with some P5.p and P7.p dividing hours after the first P6.p division (Fig. 5G). These results indicate
237 that NHR-85 functions to enhance the robustness of temporally regulated processes during
238 development and that some level of *lin-4* transcription occurs without NHR-85$^{Rev\text{-}Erb}$, perhaps driven
239 by NHR-23^{ROR} alone. Consistent with the hypothesis that NHR-23 and NHR-85 function together to
240 control the normal temporal regulation, RNAi-mediated depletion of *nhr-23* activity in wild-type
241 animals using RNAi conditions that do not induce developmental arrest result in mild heterochronic
242 phenotypes (Fig. S6). The penetrance of these phenotypes is enhanced when *nhr-23* is depleted in
243 *nhr-85(0)* animals, indicating that both NHRs also function cooperatively in temporal patterning (Fig.
244 S7).

245
246 **Discussion**
247
248 Most genetic oscillators are composed of auto-regulatory transcriptional/translational
249 feedback loops where transcription of core clock components are self-regulated (*35*). A prime
250 example of this type of regulatory circuit is the mammalian circadian clock that coordinates
251 anticipatory patterns of gene expression with the day-night cycle. Circadian transcription factors
252 CLOCK and BMAL1 generate rhythmic expression patterns of thousands of clock control genes
253 (CCGs) (*36-39*) (Fig. 5H). CCGs include two core transcriptional repressors, Period and CRY, which
254 heterodimerize to negatively regulate CLOCK/BMAL1 activity through direct physical interaction. A
255 second set of CCG repressors is encoded by two NHR genes, Rev-Erb and ROR, which dynamically
256 modulate core clock expression through opposing transcriptional activities (Fig. 5H)(*40-42*). The
257 delays in expression and translation of these sets of negative clock regulators enable this GRN
258 architecture to generate periodic transcriptional patterns of ~24hrs that are entrainable by new
259 light/dark cycles and maintain consistent periodicity in divergent environmental
260 conditions/temperatures (*43*).

261 Here, we show that *C. elegans* larvae employ a GRN involving multiple circadian-related
262 genes to couple *lin-4* transcriptional pulses to the larval molting cycle (Fig. 5H). The complement of

263 shared components between the human and *C. elegans* GRNs combined with major differences in
264 their regulatory architecture is remarkable. Primary among these differences is the absence of genes
265 encoding Clock and Bmal1 orthologs in the *C. elegans* genome. We propose here that the worm
266 orthologs of Rev-Erb and ROR, which function in humans in a purely auxiliary capacity to stabilize
267 the expression of core circadian clock components, compose the central transcription factors of the
268 hypodermal developmental clock (Fig. 5H). In contrast to their antagonistic roles in the circadian
269 clock, *C. elegans* NHR-85$^{Rev\text{-}Erb}$ and NHR-23^{ROR} heterodimerize and work cooperatively to promote
270 transcriptional pulses (Fig. 5H). Importantly, we demonstrate that cooperativity between NHR-85$^{Rev\text{-}}$
271 ^{Erb} and NHR-23^{ROR} for binding *lin-4* regulatory elements dictates the timing and duration of *lin-4*
272 transcription and that the duration of these interactions is negatively regulated by LIN-42^{Period}.
273 Specifically, LIN-42^{Period} binds to NHR-85$^{Rev\text{-}Erb}$ and controls dynamic nature of its expression. Defects
274 in *lin-42* function result in an increase in Pol II density at the *lin-4* locus and a dramatic increase in
275 the duration of *lin-4* transcriptional pulses by expanding the duration NHR-85$^{Rev\text{-}Erb}$ and NHR-23^{ROR}
276 co-expression. The resulting alterations in *lin-4* dosage (and likely the dosage of additional
277 heterochronic miRNAs) cause precocious heterochronic phenotypes in *lin-42* mutants. This suggests
278 that physical and functional interactions between Period orthologs and conserved NHRs are
279 maintained in both circadian and developmental clock systems and that other *C. elegans* NHRs, in
280 addition to NHR-85$^{Rev\text{-}Erb}$, may function in the heterochronic pathway.

281 While NHR-85$^{Rev\text{-}Erb}$ and NHR-23^{ROR} generate pulses of *lin-4* transcription in the hypodermis,
282 NHR-23^{ROR} may coordinate cyclical gene expression patterns with overall animal development (Fig.
283 2A). *nhr-23* is an essential gene and *nhr-23(0)* animals arrest during late embryogenesis/hatching at
284 a time when oscillatory transcription begins (*8, 9, 44*). Depletion of NHR-23^{ROR} during post-embryonic
285 development results in highly penetrant larval arrest phenotypes (*45*). These arrests prevent somatic
286 cell proliferation/differentiation, occur at the beginning of each larval stage and correlate with the
287 developmental period where NHR-23^{ROR} expression begins (*45*). While the general suspension of
288 developmental processes in NHR-23^{ROR}-depleted animals make it unfeasible to measure direct
289 changes in transcription for individual genes, these arrests resemble post-embryonic developmental
290 checkpoints where somatic cell proliferation and cyclical gene expression patterns (including *lin-4*)
291 are halted during acute food removal/starvation (*11, 46*). Starvation-induced checkpoints are
292 mediated through regulation of the conserved insulin signaling pathway which generate a variety of
293 sterol-derived hormones (*47*). These hormones may serve as ligands for individual NHRs and provide
294 a mechanism to organize global patterns of gene expression and regulate the pace of organismal
295 development with the molting cycle.

REFERNCES

1. J. E. Sulston, H. R. Horvitz, *Developmental biology* **56**, 110-156. (1977).
2. V. Ambros, H. R. Horvitz, *Science* **226**, 409-416 (1984).
3. A. E. Rougvie, E. G. Moss, *Curr Top Dev Biol* **105**, 153-180 (2013).
4. R. Feinbaum, V. Ambros, *Developmental biology* **210**, 87-95. (1999).
5. M. Li *et al.*, *Developmental cell* **9**, 415-422 (2005).
6. P. M. Van Wynsberghe, A. E. Pasquinelli, *Worm* **3**, e974453 (2014).
7. R. Perales *et al.*, *PLoS genetics* **10**, e1004486 (2014).
8. G.-J. Hendriks *et al.*, *Mol Cell* **53**, 380-392 (2014).
9. M. W. Meeuse *et al.*, *Mol Syst Biol* **16**, e9498 (2020).
10. D. h. Kim *et al.*, *Nat Genet* **45**, 1337-1344 (2013).
11. N. Stec *et al.*, *Curr Biol* **31**, 809-826 e806 (2021).
12. K. A. McCulloch, A. E. Rougvie, *Proceedings of the National Academy of Sciences of the United States of America* **111**, 15450-15455 (2014).
13. R. Patel *et al.*, *Elife* **11**, (2022).
14. C. M. Hammell *et al.*, *PNAS* **106**, 18668-18673 (2009).
15. A. Bethke *et al.*, *Science* **324**, 95-98 (2009).
16. M. C. Ow *et al.*, *Genes & development* **22**, 2520-2534 (2008).
17. S. F. Roush, F. J. Slack, *Developmental biology* **334**, 523-534 (2009).
18. M. W. M. Meeuse *et al.*, *bioRxiv*, (2022).
19. R. C. Lee *et al.*, *Cell* **75**, 843-854. (1993).
20. E. Tutucci *et al.*, *Nat Methods* **15**, 81-89 (2018).
21. J. R. Bracht *et al.*, *Developmental biology* **348**, 210-221 (2010).
22. W. Keil *et al.*, *Developmental cell*, (2016).
23. D. R. Larson *et al.*, *Trends in cell biology* **19**, 630-637 (2009).
24. B. M. Forman *et al.*, *Cell* **81**, 541-550 (1995).
25. T. Perlmann *et al.*, *Mol Endocrinol* **10**, 958-966 (1996).
26. F. Rastinejad *et al.*, *Nature* **375**, 203-211 (1995).
27. T. P. Burris, *Mol Endocrinol* **22**, 1509-1520 (2008).
28. P. M. Van Wynsberghe *et al.*, *Developmental biology* **390**, 126-135 (2014).
29. J. Cao *et al.*, *Science* **357**, 661-667 (2017).
30. D. Z. L. Mok *et al.*, *BMC developmental biology* **15**, 26 (2015).
31. M. Jeon *et al.*, *Science* **286**, 1141-1146 (1999).
32. J. M. Tennessen *et al.*, *Developmental biology* **289**, 30-43 (2006).
33. J. E. Abrahante *et al.*, *Genetics* **149**, 1335-1351 (1998).
34. I. Schmutz *et al.*, *Genes Dev* **24**, 345-357 (2010).
35. B. Novak, J. J. Tyson, *Nat Rev Mol Cell Biol* **9**, 981-991 (2008).
36. M. K. Bunger *et al.*, *Cell* **103**, 1009-1017 (2000).
37. J. B. Hogenesch *et al.*, *Proc Natl Acad Sci U S A* **95**, 5474-5479 (1998).
38. D. P. King *et al.*, *Cell* **89**, 641-653 (1997).
39. M. Reick *et al.*, *Science* **293**, 506-509 (2001).
40. N. Preitner *et al.*, *Cell* **110**, 251-260 (2002).
41. H. R. Ueda *et al.*, *Nature* **418**, 534-539 (2002).
42. T. K. Sato *et al.*, *Neuron* **43**, 527-537 (2004).
43. P. Francois *et al.*, *PLoS Comput Biol* **8**, e1002585 (2012).
44. M. Kostrouchova *et al.*, *PNAS* **98**, 7360-7365 (2001).
45. L. C. Johnson *et al.*, *bioRxiv*, 2021.2010.2027.465992 (2022).
46. A. J. Schindler *et al.*, *PLoS genetics* **10**, e1004426 (2014).

47. L. R. Baugh, P. J. Hu, *Genetics* **216**, 837-878 (2020).

Acknowledgements:

We would like to thank M. Walhout, J. Ward, J. Kimble for strains and reagents and D. Matus and T. Medwig-Kinney for help with confocal imaging. We would like to also thank G. Sumati for help with recombinant protein expression. L.J. is an investigator of the Howard Hughes Medical Institute. We acknowledge T. Medwig-Kinney, C. Vakoc, R. Martienssen, U. Pedmale, and D. Jackson for suggestions throughout the course of this study.

Funding:

National Institutes of Health R01GM117406 (CMH, NS, KH-M)

National Science Foundation 2217560 (CMH, JW)

CSHL Cancer Training Grant T32CA148056 (BK)

The CNRS ATIP/Avenir program Conseil Regional d'Île de France (DIM ELICIT-AAP-2020 KEIL) (20002719) (WK)

Fondation pour la Recherche Médicale FDT202204015083 (SS)

Howard Hughes Medical Institute (LJ, DA, MJ)

Author Contributions:

Conceptualization: CMH, BK, SS, WK

Methodology: BK, SS, NS, KH-M, DA, JW, MJ, LJ, WK, CMH

Investigation: BK, SS, DA, NS, KH-M, WK, CMH

Visualization: CMH, WK, BK, SS

Funding acquisition: CMH, WK, JT

Project administration: CMH, WK

Supervision: CMH, WK, JT

Writing – original draft: CMH

Writing – review & editing: CMH, WK, BK

Competing interests: All authors declare no competing interests.

373 **Data and materials availability:** Strains and plasmids listed in the Supplementary Materials and
374 Methods Section are available through the *Caenorhabditis Genetics* Center or by request to C.M.H..
375 The authors affirm that all data necessary for confirming the conclusions of the article are present
376 within the article, figures, and tables.

377 **Supplementary Materials**

378 Materials and Methods

379 Figs. S1-S6

380 Tables S1-S4

381 References (*1-17*)

382 Movies S1-S2

383

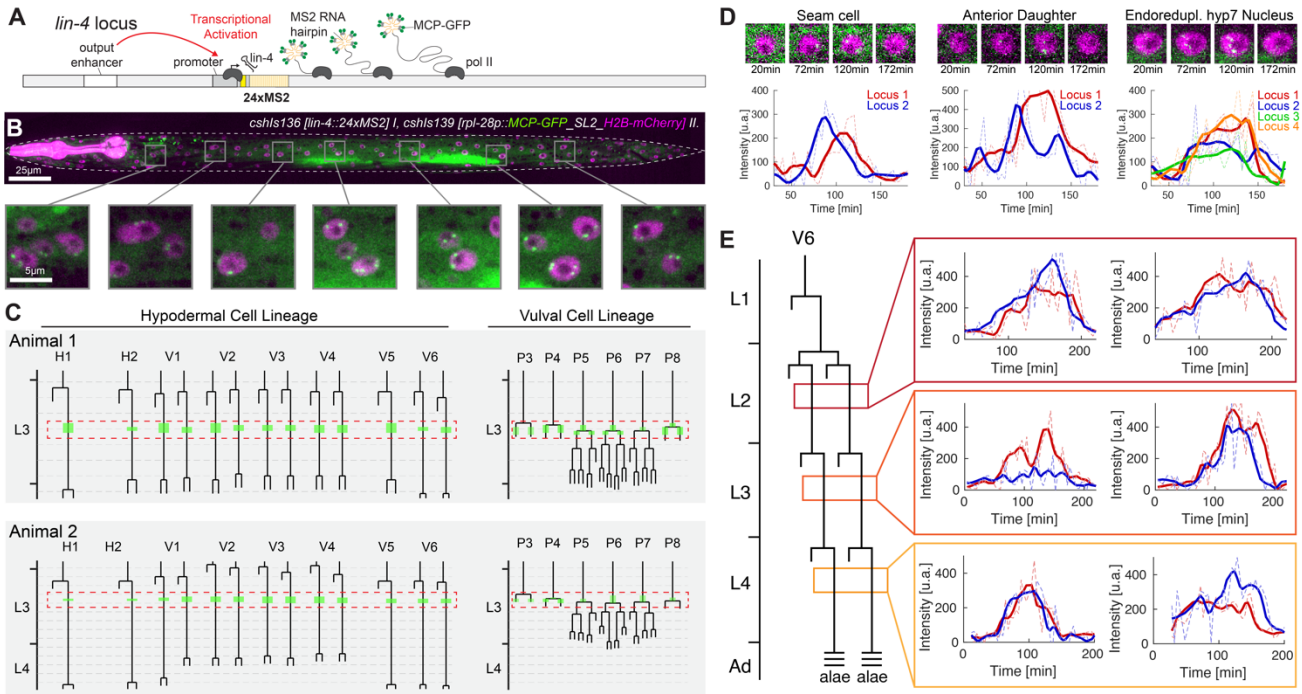

Fig. 1. *lin-4* transcription is highly pulsatile at each larval stage. (**A**) The MS2/MCP system is composed of a MS2 coat protein GFP fusion (MCP-GFP) which can bind to MS2 RNA hairpins encoded within primary miRNA transcripts. (**B**) Image of mid-L3 staged larva and magnified insets showing MCP-GFP spots in hypodermal cells along the anteroposterior axis. (**C**) Two examples of L3/L4 hypodermal and vulval precursor cell lineages, with overlayed expression patterns indicating when MCP-GFP foci were visible in each lineage. (**D**) Snapshots of individual seam cell and hyp7 cell expression trajectories from L3-staged animals. (**E**) Expression traces in pairs of V6.p seam cells from L2, L3, and L4 staged animals.

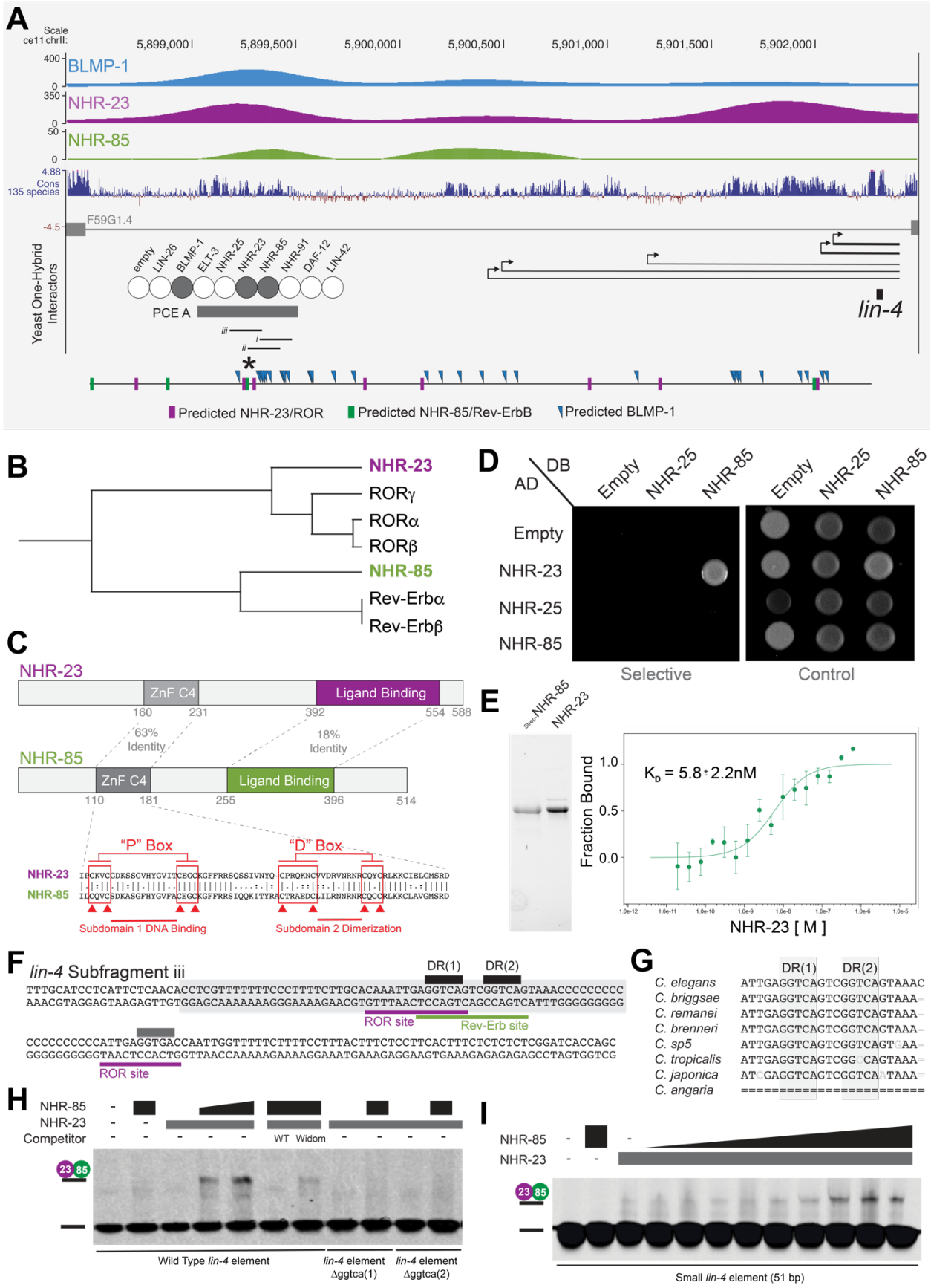
A
Scale
ce11 chrII:
5,899,000
5,899,500
5,900,000
5,900,500
5,901,000
5,901,500
5,902,000
BLMP-1
NHR-23
NHR-85
Cons
135 species
F59G1.4
Yeast One-Hybrid Interactors
empty
LIN-26
BLMP-1
ELT-3
NHR-25
NHR-23
NHR-85
NHR-91
DAF-12
LIN-42
PCE A
lin-4
Predicted NHR-23/ROR
Predicted NHR-85/Rev-ErbB
Predicted BLMP-1
B
NHR-23
RORγ
RORα
RORβ
NHR-85
Rev-Erbα
Rev-Erbβ
C
NHR-23
ZnF C4
Ligand Binding
160
231
392
554
588
63% Identity
18% Identity
NHR-85
ZnF C4
Ligand Binding
110
181
255
396
514
"P" Box
"D" Box
NHR-23
NHR-85
Subdomain 1 DNA Binding
Subdomain 2 Dimerization
D
AD
DB
Empty
NHR-25
NHR-85
Empty
NHR-23
NHR-25
NHR-85
Selective
Control
E
Strep
NHR-85
NHR-23
Fraction Bound
1.0
0.5
0.0
K_D = 5.8 ± 2.2nM
1.0e-12
1.0e-11
1.0e-10
1.0e-9
1.0e-8
1.0e-7
1.0e-6
1.0e-5
NHR-23 [M]
F
lin-4 Subfragment iii
DR(1)
DR(2)
TTTGCATCCTCATTCTCAACACCTCGTTTTTTTCCCTTTTCTTGCACAAATTGAGGTCAGTCGGTCAGTAAACCCCCCCCC
AAACGTAGGAGTAAGAGTTGTGGAGCAAAAAAAGGGAAAAGAACGTGTTTAACTCCAGTCAGCCAGTCATTTGGGGGGGGG
ROR site
Rev-Erb site
CCCCCCCCCCATTGAGGTGACCAATTGGTTTTTCTTTTCCTTTACTTTCTCCTTCACTTTCTCTCTCTCGGATCACCAGC
GGGGGGGGGGTAACTCCACTGGTTAACCAAAAAGAAAAGGAAATGAAAGAGGAAGTGAAAGAGAGAGAGCCTAGTGGTCG
ROR site
G
DR(1)
DR(2)
C. elegans ATTGAGGTCAGTCGGTCAGTAAAC
C. briggsae ATTGAGGTCAGTCGGTCAGTAAA-
C. remanei ATTGAGGTCAGTCGGTCAGTAAA-
C. brenneri ATTGAGGTCAGTCGGTCAGTAAA-
C. sp5 ATTGAGGTCAGTCGGTCAGT-AA-
C. tropicalis ATTGAGGTCAGTCGG-CAGTAAA-
C. japonica AT-GAGGTCAGTCGGTCA-TAAA-
C. angaria ==========
H
NHR-85
NHR-23
Competitor
WT
Widom
23
85
Wild Type lin-4 element
lin-4 element Δggtca(1)
lin-4 element Δggtca(2)
I
NHR-85
NHR-23
23
85
Small lin-4 element (51 bp)

394

395 **Fig. 2. NHR-85$^{Rev\text{-}Erb}$ and NHR-23^{ROR} form a heterodimeric complex that binds cooperatively to**
396 **regulatory elements controlling pulsatile *lin-4* transcription.** (**A**) BLMP-1, NHR-85 and NHR-23
397 bind to the *lin-4* PCE in one-hybrid assays (*11*). Browser tracks showing BLMP-1, NHR-23 and NHR-
398 85 bindings sites near the *lin-4* locus. Also indicated are the major *lin-4* pri-miRNAs (*21*), the
399 computationally defined binding sites for each TF, and the sub-fragments of the *lin-4* PCE element
400 used in gel shifts below. Asterisk indicates location of the direct repeats of GGTCA in PCE element.
401 (**B**) Sequence relationships between NHR-23 and NHR-85 and human Rev-Erb and ROR. (**C**) NHR-
402 23^{ROR} and NHR-85$^{Rev\text{-}Erb}$ domain organization highlighting similarity in DNA binding domains. (**D**)
403 NHR-23^{ROR} and NHR-85$^{Rev\text{-}Erb}$ interact with each other in two-hybrid assays. (**E**) Recombinant, purified
404 strep-NHR-85$^{Rev\text{-}Erb}$ and NHR-23^{ROR} interact in MST binding assays. (**F**) Sequences of the PCE sub-
405 fragment iii from A and the 51bp minimal binding element (grey box) derived from *lin-4* PCEiii. (**G**)
406 Conservation of the direct repeats DRs in the PCE elements of different nematode species. (**H** and **I**)
407 EMSA experiments of wild-type and mutant target DNAs using recombinant NHR-85$^{Rev\text{-}Erb}$ and NHR-
408 23^{ROR}.
409

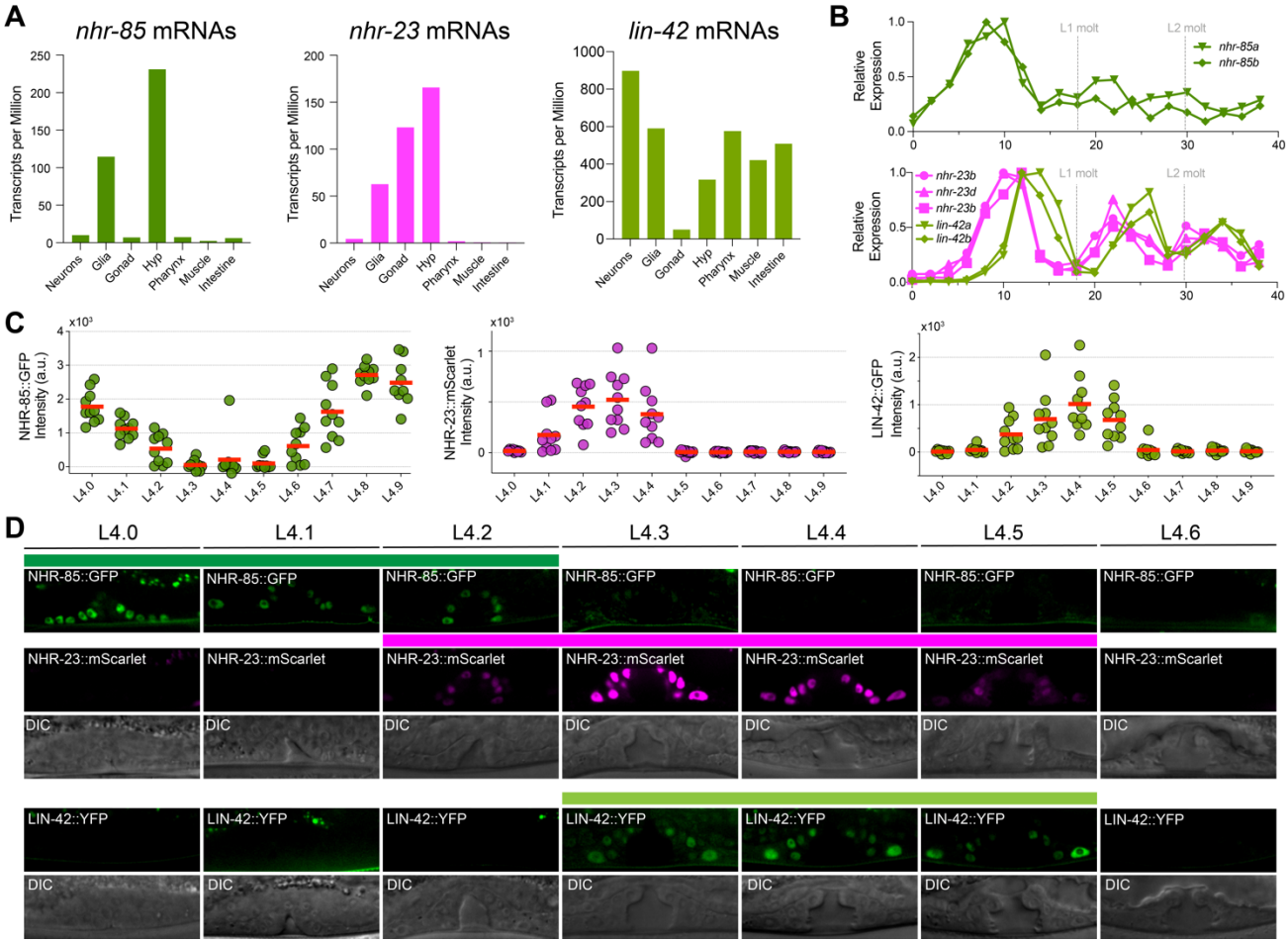

Fig. 3. NHR-85$^{Rev\text{-}Erb}$, NHR-23^{ROR}, and LIN-42^{Period} exhibit phased, overlapping expression patterns. (**A**) Single-cell mRNA expression analysis of *nhr-85, nhr-23,* and *lin-42* transcripts from L2 staged animals. (**B**) RNA-seq time course data of *nhr-85, nhr-23,* and *lin-42* mRNA expression patterns. (**C-D**) Quantification (C) and micrographs (D) depicting NHR-85$^{Rev\text{-}Erb}$::GFP, NHR-23^{ROR}::mScarlet, and LIN-42^{Period}::YFP expression in hypodermal seam cells and vulval cells, respectively, in each morphologically defined L4 substage (*30*). Circles represent individual animals (3 cells sampled); red bars indicate the mean. Colored bars indicate ranges of detectable expression.

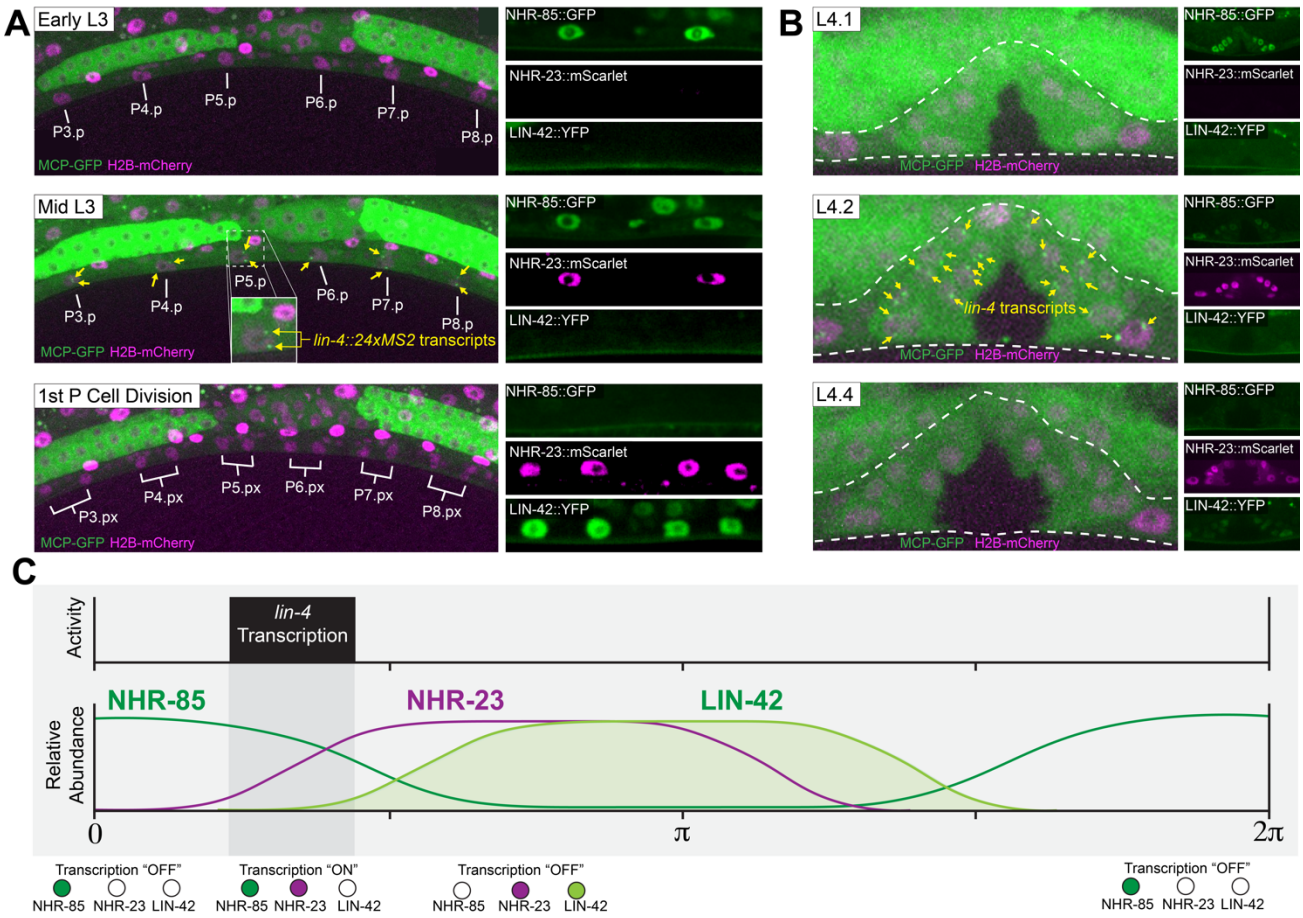

Fig. 4. *lin-4* transcription occurs during periods where NHR-85$^{Rev\text{-}Erb}$::GFP and NHR-23^{ROR}::mScarlet are co-expressed and LIN-42^{Period}::YFP and NHR-85$^{Rev\text{-}Erb}$::GFP exhibit antiphasic expression patterns. (**A**) Time course experiments of MCP-GFP demonstrate that *lin-4::24xMS2* expression occurs immediately before the first Pn.p cell divisions and not until NHR-85$^{Rev\text{-}Erb}$::GFP are NHR-23^{ROR}::mScarlet are co-expressed in the vulval precursor cells. *lin-4::24xMS2* expression terminates by the time NHR-85$^{Rev\text{-}Erb}$::GFP expression is extinguished in second division VPC. The cessation of *lin-4::24xMS2* expression corresponds to time when LIN-42^{Period}::YFP accumulates in these cells. (**B**) The dynamics of *lin-4::24xMS2* transcription in L4 staged vulvas. *lin-4::24xMS2* expression occurs at the same developmental stage were NHR-85$^{Rev\text{-}Erb}$::GFP and NHR-23^{ROR}::mScarlet co-expressed. As with L3-stage expression of *lin-4::24xMS2,* MCP-GFP foci are diminished around the onset time of LIN-42^{Period}::YFP expression. (**C**) Image summarizing the relationship between dynamic expression patterns of NHR-85$^{Rev\text{-}Erb}$, NHR-23^{ROR}, and LIN-42^{Period} with the period of *lin-4* transcriptional activation in the L3/L4 stages.

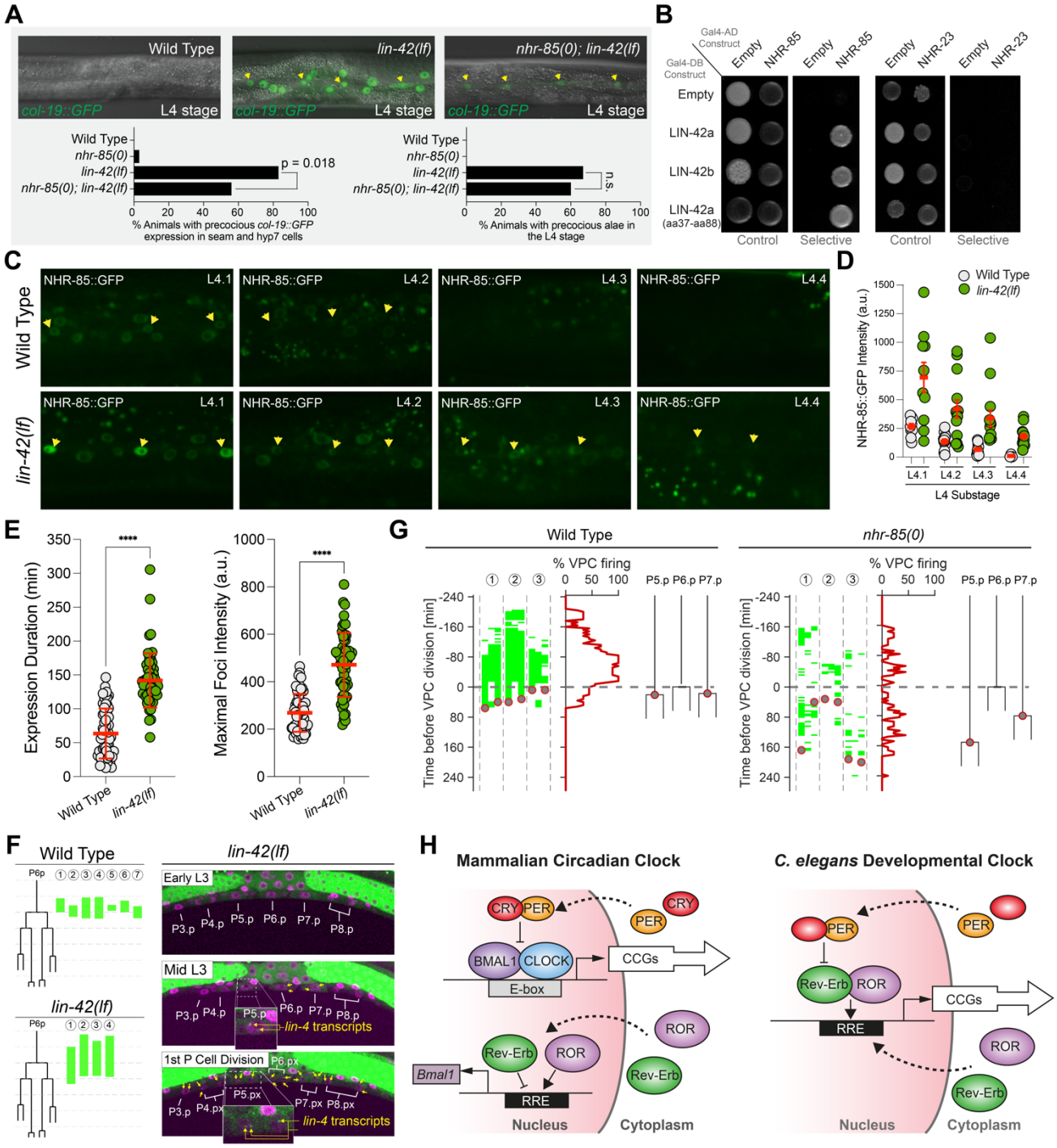

Fig. 5. LIN-42^{Period} binds to and regulates the expression dynamics of NHR-85 to control the amplitude and duration of *lin-4* transcription. (**A**) *lin-42(lf)* mutants express *col-19::GFP* during the L3 stage of development and deletion of *nhr-85(0)* suppresses these phenotypes. Yellow arrows indicate the lateral seam cells of L4-staged animals. Error bars were calculated using two-tailed chi-square analysis. (**B**) LIN-42 isoforms interact with NHR-85$^{Rev\text{-}Erb}$ but not NHR-23^{ROR} in two-hybrid assays. (**C and D**) Representative images and quantification of NHR-85$^{Rev\text{-}Erb}$::GFP expression

441 dynamics in hypodermal cells of L4-staged wild-type and *lin-4(lf)* animals. Yellow arrows indicate the
442 lateral seam cells of L4-staged animals. Circles represent average expression in three seam cells of
443 an individual animal. Error bars show mean and standard deviation. Significance calculated using
444 Welch's t-test. (**E**) Quantification of the duration and intensity of MCP-GFP foci in L3-staged animals.
445 Error bars and significance calculated as in D. (**F**) Time course analysis of the onset/offset times for
446 MCP-GFP foci in VPCs of wild-type and *lin-42(lf).* Green lines indicate timing of *lin-4::24xMS2*
447 expression in P6.p cells of individual animals. Pictographs show a representative image of the ventral
448 surface of a single *lin-42(lf)* animal throughout the time course. (**G**) High-resolution time course
449 analysis of *lin-4::24xMS2* expression in wild-type and *nhr-85(0)* mutants, aligned to first P6.p cell
450 division (t=0). Green areas indicate detectable MCP-GFP foci in individual P cells (P5.p – P7.p) (n =
451 3 animals). Grey circles represent the timing of P5.p and P7.p divisions. (**H**) Model of the mammalian
452 circadian clock and *C. elegans* developmental clock uncovered in this study.
453

454 **Supplemental Information to Accompany**

455

456

457 **Circadian rhythm orthologs drive pulses of heterochronic miRNA transcription in *C. elegans***

458

459 Brian Kinney[1]*, Shubham Sahu[2]*, Natalia Stec[1], Kelly Hills-Muckey[1], Dexter W. Adams[3,4], Jing
460 Wang[1], Matt Jaremako[3], Leemor Joshua-Tor[3], Wolfgang Keil[2,†] , Christopher M. Hammell[1,†]

461

462

463 [1]Cold Spring Harbor Laboratory, Cold Spring Harbor, NY 11724, USA.

464 [2]Institut Curie, Université PSL, Sorbonne Université, CNRS UMR168 Laboratoire Physico Chimie
465 Curie, 75005 Paris, France.

466 [3]Howard Hughes Medical Institute, W. M. Keck Structural Biology Laboratory, Cold Spring Harbor
467 Laboratory, Cold Spring Harbor, NY, 11724, USA

468 [4]Graduate Program in Genetics, Stony Brook University; Stony Brook, NY 11794, USA

469

470 *These authors contributed equally

471 [†]Correspondence: wolfgang.keil@curie.fr (W.K.); chammell@cshl.edu (C.M.H.) (lead contact)

472

473

474 **SUPPLEMENTAL FIGURES:**

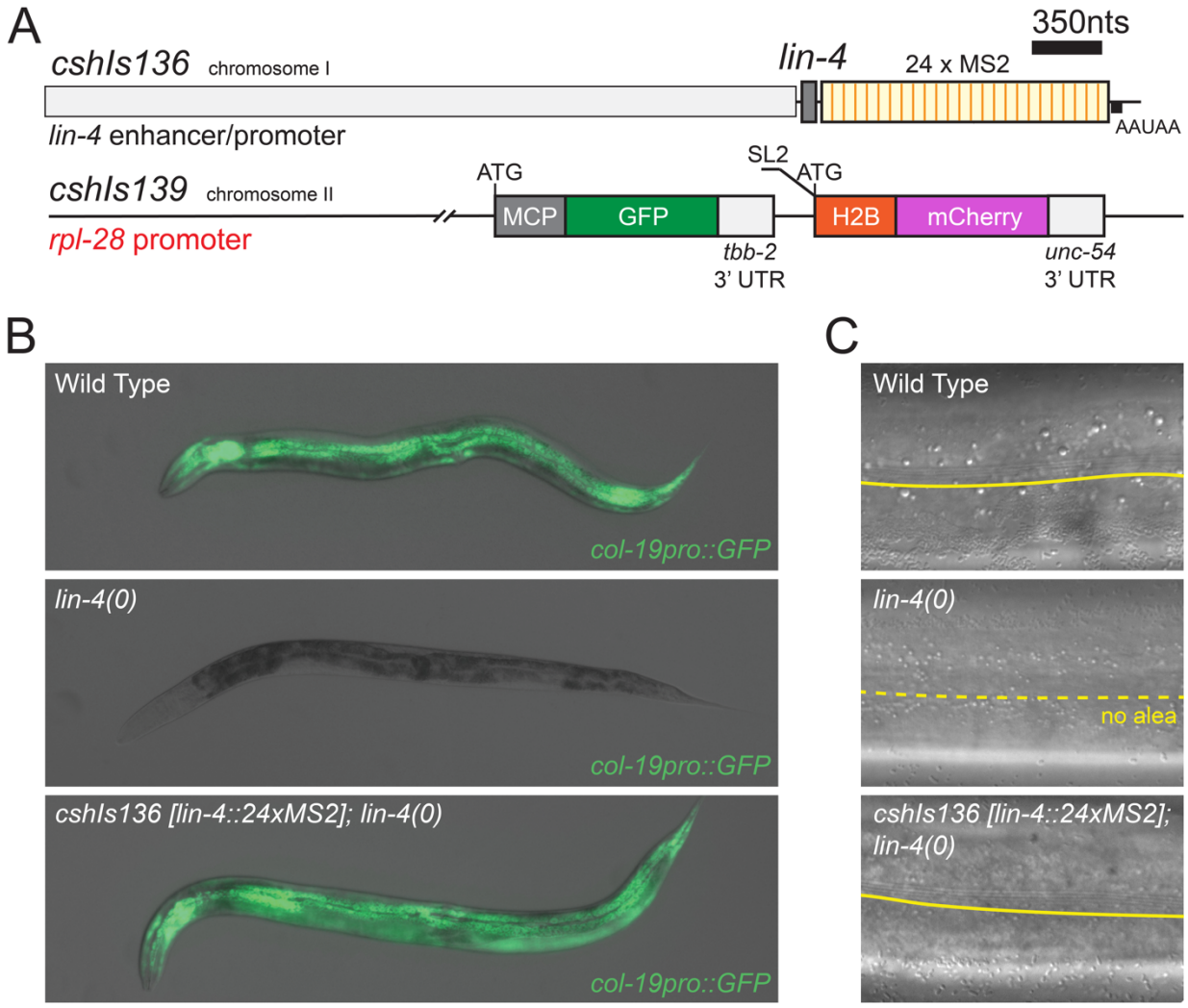

475

476 **Fig. S1. The single copy, MS2-tagged *lin-4* transgene rescues *lin-4* temporal patterning**
477 **defects.** (**A**) Wild-type animals express a *col-19::GFP* transgene immediately after the L4 molt
478 (100%; n = 50) while *lin-4(e912)* mutants fail to induce *col-19::GFP* expression (0% expressing; n =
479 43). *cshIs136 [lin-4::24xMS2; unc-119(+) I; lin-4(e912) I]* animals exhibit normal *col-19::GFP*
480 expression (100% expressing; n = 30). (**B**) Wild-type animals generate adult-specific alae structures
481 on the cuticles of young adult animals (100%; n = 23). 100% (n = 40) of *lin-4(e912)* animals lack these
482 structures. *cshIs136 [lin-4::24xMS2; unc-119(+) I; lin-4(e912) I*] animals exhibit wild-type adult alae
483 (100%; n = 40).

484

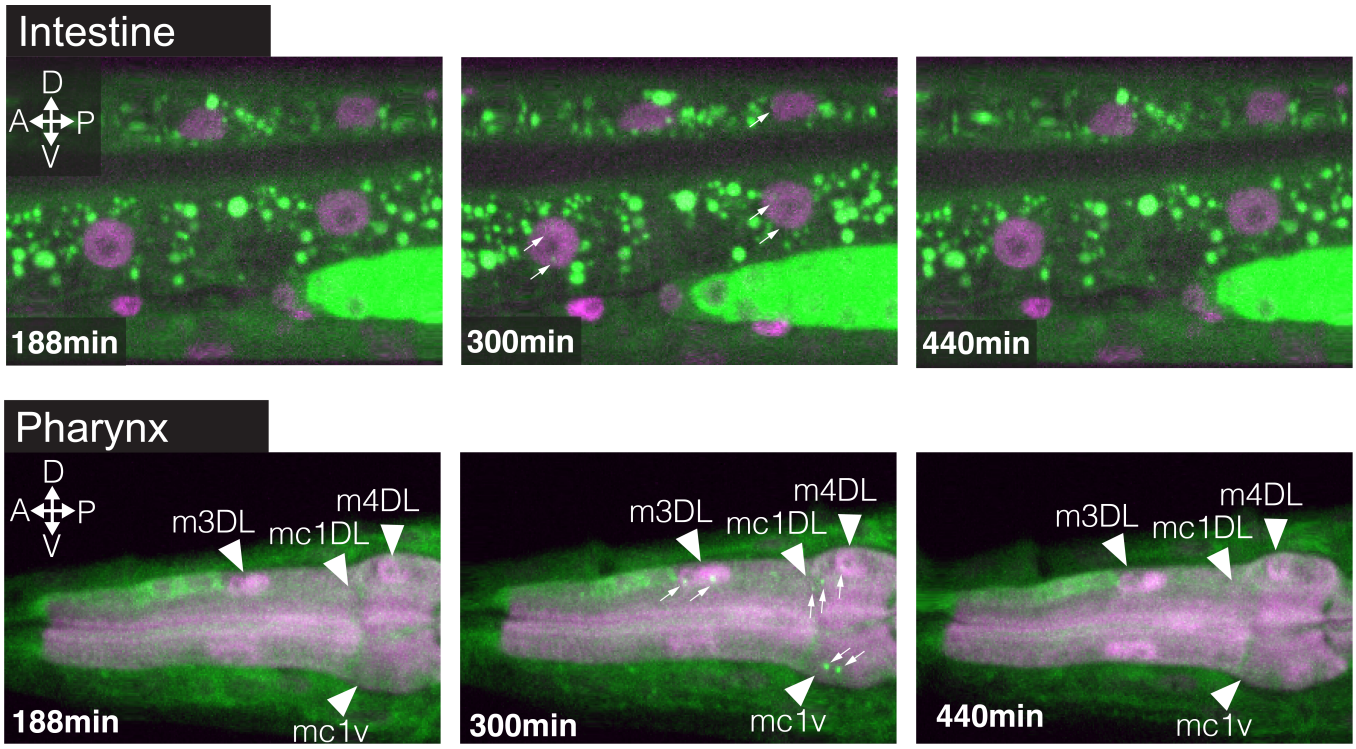

Fig. S2. *lin-4::24xMS2* expression is pulsatile in other somatic cells. Timeseries of *lin-4::24xMS2* expression in intestine cells and cells of the pharynx in L3-staged animals. Small arrows indicate MCP-GFP foci and triangles indicate the location of the indicated cell.

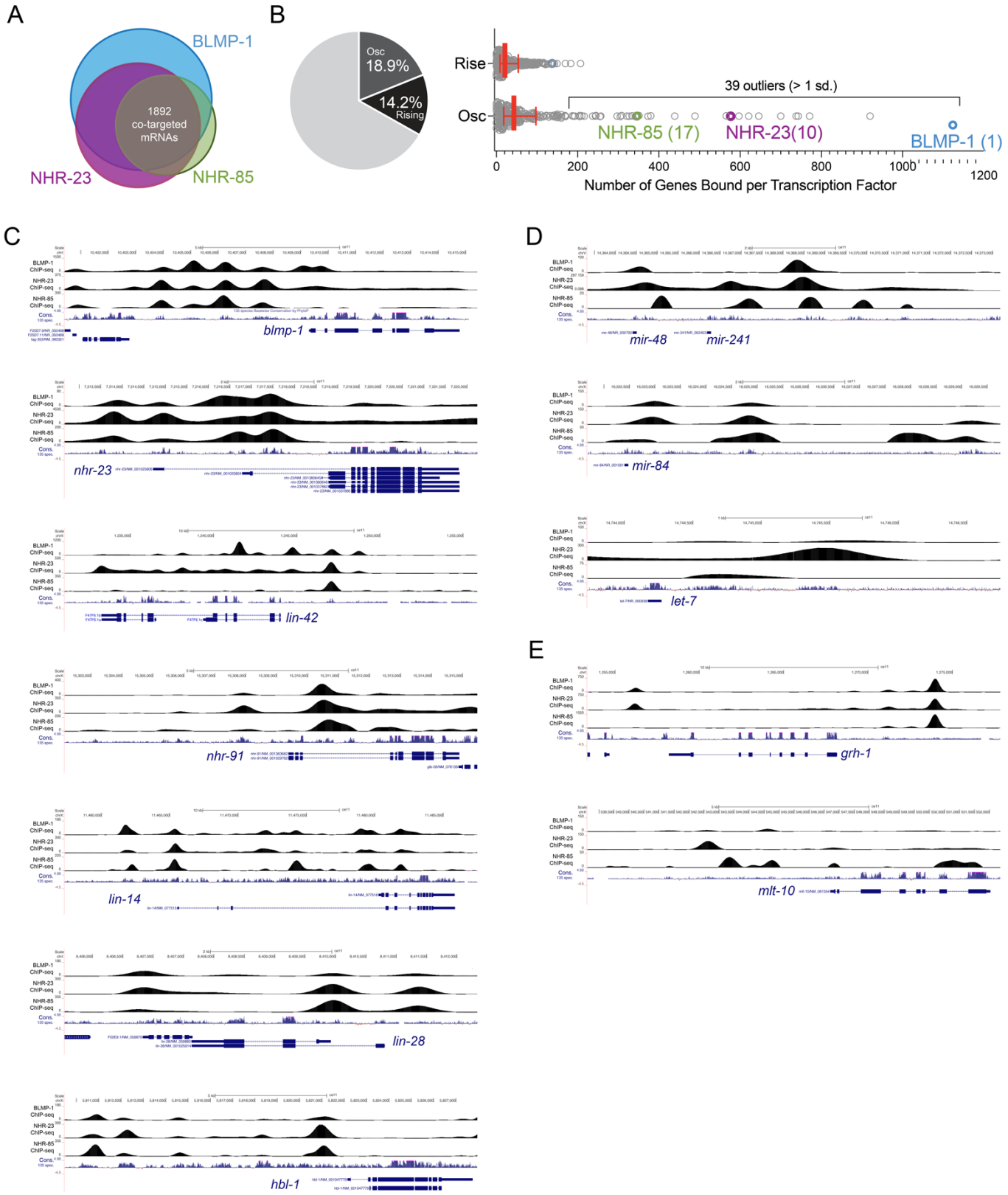

490

491 **Fig. S3. BLMP-1, NHR-23^{ROR}, and NHR-85$^{Rev\text{-}Erb}$ binding sites are enriched in the promoters of**

492 **cyclically transcribed genes as well as genes that function in the heterochronic pathway.** (**A**)

493 Venn diagram indicating the level of overlap of genes targeted by BLMP-1, NHR-85 and NHR-23.
494 For this analysis, peaks from NHR-85$^{Rev\text{-}Erb}$, NHR-23^{ROR} and BLMP-1 ChIP-seq experiments were
495 assigned to the nearest proximal protein coding genes (+3kb upstream and 300bp downstream)
496 (Tables S1 and S2). (**B**) NHR-85$^{Rev\text{-}Erb}$, NHR-23^{ROR} and BLMP-1 binding sites are enriched in the
497 promoters of genes that exhibit oscillatory expression patterns. Calculations were derived from
498 population-based RNA-seq time course data sets (*8*) that partition the expression of post-
499 embryonically expressed genes into three types: (i) transcripts with their transcriptional periodicity
500 tied to the molting cycle (osc; 18.9%; 2,718 of 14,378 total genes) (ii) genes with rising expression
501 throughout larval development (rising; 14.2%) and (iii) genes with flat expression profile (flat; 66.9%)
502 (Fig. 2E). Using these data sets, we compared the numbers of cyclically expressed genes that were
503 targeted by NHR-85$^{Rev\text{-}Erb}$ or NHR-23^{ROR} to those targeted by any of the other 170 TFs queried in by
504 the *C. elegans* ModEncode Project (using 265 publicly available, validated ModEncode ChIP-seq
505 data-sets (tables S1 and S2)(*48*). (**C**) Browser tracks overlaying the BLMP-1, NHR-23^{ROR}, and NHR-
506 85$^{Rev\text{-}Erb}$ ChIP-seq signal near the indicated loci.

507

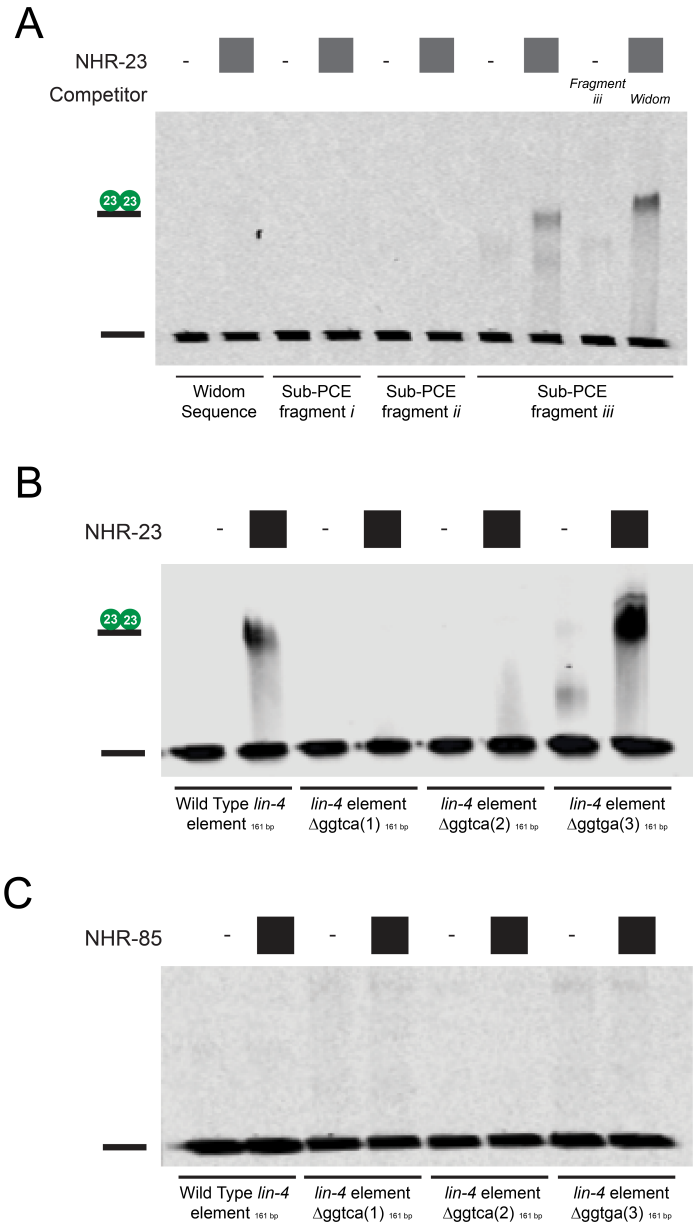

Fig. S4. NHR-23^{ROR} can bind the *lin-4* sub-fragment III at high protein concentrations while NHR-85$^{Rev\text{-}Erb}$ cannot. (**A**) NHR-23^{ROR} can bind specifically to PCE sub-fragment III that contains both direct repeats outlined in Fig. 2F and G. (**B**) NHR-23^{ROR} binding to the PCE sub-fragment III requires the two direct repeats but does not require the un-conserved single GGTGA element downstream of the direct repeats (see Fig. 2 for details). (**C**) NHR-85$^{Rev\text{-}Erb}$ does not bind to any of the PCE sub-elements to any appreciable degree.

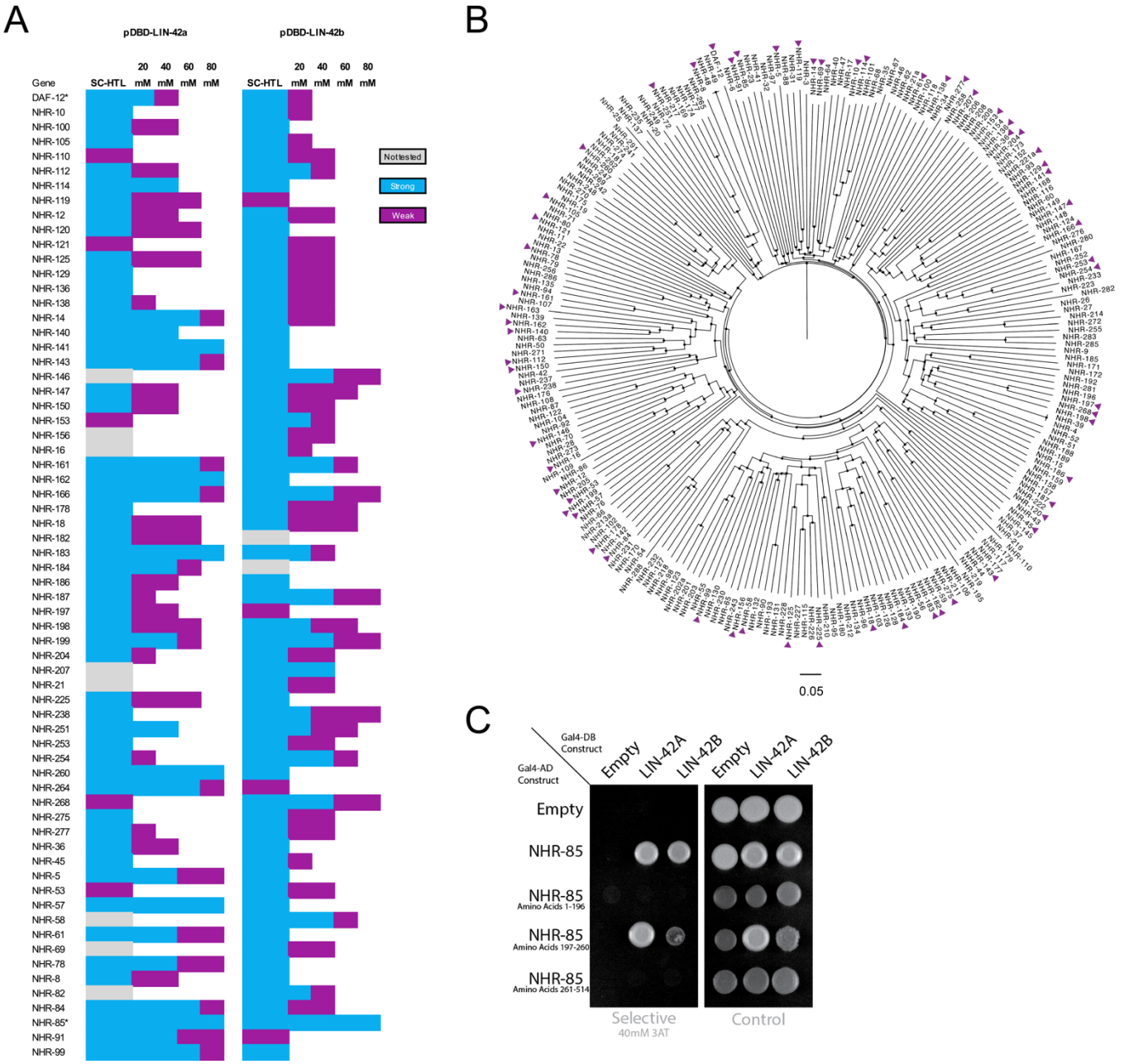

Fig. S5. LIN-42^{Period} interacts with multiple C. elegans NHRs and interacts with NHR-85$^{Rev\text{-}Erb}$ via the hinge region that separates the DNA-binding domain and ligand-binding domain. (**A**) A list depicting the NHRs that interact with one of the two two-hybrid baits for LIN-42 (LIN-42a and LIN-42b isoforms). Colors indicate the level of yeast growth solid growth media containing the indicated concentration of 3-AT. (**B**) Dendrogram of *C. elegans* nuclear hormone receptors showing the relationships between conserved sub-families of NHRs and the distribution of LIN-42 interactions within this large family of TFs. Purple triangles indicate NHRs that interact with one or both LIN-42

524 isoforms. (**C**) Two hybrid results that indicate that both LIN-42 isoforms can interact with the central
525 hinge region of NHR-85.

526

527

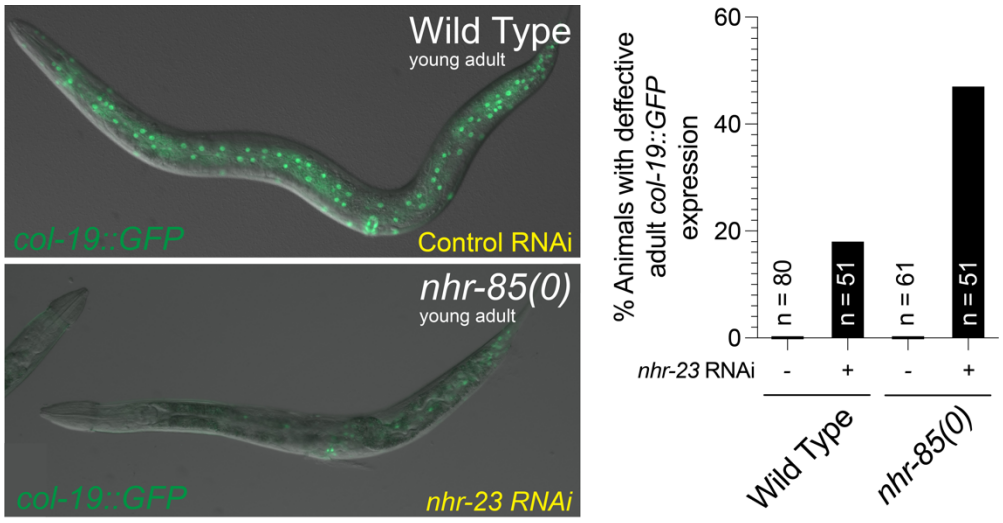

528 **Fig. S6. Depletion of nhr-23 results in defects in expressing adult-specific GFP reporters after**
529 **the L4 molt.** The adult-specific *col-19::GFP* reporter is expressed in both seam and hyp7 cells in
530 wild-type animals. Depletion of *nhr-23* prevents normal expression of *col-19::GFP* during adulthood.
531 In *nhr-23* RNAi treated animals, the indicated percentage of animals expressed *col-19::GFP* in the
532 head and tail cells of the hypodermis. The reduction of *col-19::GFP* expression in young adult animals
533 is stronger in animals lacking *nhr-85*. *nhr-23* RNAi cultures were diluted to 50% with control RNAi
534 bacteria to enable animals to develop to adulthood and avoid the fully penetrant larval arrest
535 phenotypes associated with undiluted *nhr-23* RNAi cultures.

536

537

538

539

540

541

542

543 **MATERIALS AND METHODS:**

544 ***C. elegans* maintenance and genetics.** *C. elegans* strains were maintained on standard media at
545 20°C and fed *E. coli* OP50 (*49*). Some strains were provided by the CGC, which is funded by NIH
546 Office of Research Infrastructure Programs (P40 OD010440). A complete list of strains is outlined in
547 Table S3.

548

549 **RNAi Feeding.** RNAi by feeding was performed using *E. coli* HT115 expressing double stranded
550 RNA corresponding to the indicated target gene or containing a control dsRNA expression plasmid
551 that does not contain sequences corresponding to any *C. elegans* gene (*50, 51*). To prevent
552 contamination by *E. coli* OP50, L4-staged animals were added to RNAi plates individually after
553 removing co-transferred bacteria. For RNAi against *nhr-23*, bacterial cultures were diluted with control
554 RNAi cultures at the indicated levels prior to experimental onset. In experiments in Fig. S6, starved
555 L1 animals of the indicated genotypes were used. Unless otherwise noted, F1 progeny were analyzed
556 for RNAi-induced phenotypes in the following 2-4 days. Plasmids used for RNAi are outlined in Table
557 S4.

558

559 **CRISPR genome editing.** Genome editing and transgene insertion was accomplished using
560 standard CRISPR/Cas9-mediated genomic editing to the ttTi5605 or ttTi4348 landing site following
561 standard protocols (*52*). For CRISPR/Cas9 editing of the endogenous *lin-42* gene, pCMH1434
562 (expressing Cas9 and a synthetic CRISPR guide RNA targeting a genomic region encoding the LIN-
563 42 C-terminus) and pCMH1439 (encoding a LIN-42::YFP fragment) were injected in to N2 animals
564 and screened by PCR to identify transgene insertion at the *lin-42* gene. Plasmids used to generate
565 CRISPR alleles are outlined in Table S4.

566

567 **Microfluidics and long-term imaging.** For microfluidics experiments, early to mid L1-staged
568 animals were isolated 6h after starvation-induced L1 arrest at 20°C before an experimental time
569 course. Other stages were individually isolated by observing defined cellular and morphological
570 features indicative of animals developmental stage (*1*). Animals were mounted into the microfluidic
571 device as previously described (*22*). During the imaging process, animals were constantly fed NA22
572 *E. coli* suspended in S medium. The temperature was kept constant at 20˚C both, at the objective
573 and the microfluidic device using a custom-built water-cooled aluminum ring (for objective) and
574 custom-built aluminum stage inset that was directly coupled to a thermal Peltier device.

575

576 **Image acquisition.** MS2-MCP-GFP live imaging Live imaging was performed with a 60x, 1.2NA
577 objective on a Nikon Ti2 Eclipse microscope equipped with a V3 CREST spinning disk confocal
578 module. To ensure fast multichannel acquisition, hardware triggering was implemented between a
579 MadCityLabs NANO Z200-N piezo z-stage, a Photometrics Prime 95B sCMOS camera with 25mm
580 field of view (2048x2048 pixels, pixel size 11um corresponding to 183nm), and a Lumencor© Celesta
581 solid-state laser source via a National Instruments (NI) PCIe-6323 card. Laser wavelengths of 488nm
582 and 545nm were used to excite MCP-GFP and histone-mCherry, respectively. Acquiring a dual-color
583 z-stack with 51 slices and 50ms exposure times takes approximately 3.2 seconds with this setup.

584

585 Confocal Microscopy: Images were acquired using a Hamamatsu Orca EM-CCD camera and a
586 Borealis-modified Yokagawa CSU-10 spinning disk confocal microscope (Nobska Imaging, Inc.) with
587 a Plan-APOCHROMAT x 100/1.4 or 40/1.4 oil DIC objective controlled by MetaMorph software
588 (version: 7.8.12.0). Animals were anesthetized on 5% agarose pads containing 10mM sodium azide
589 and secured with a coverslip. Imaging on the microfluidic device was performed on a Zeiss AXIO
590 Observer.Z7 inverted microscope using a 40X glycerol immersion objective and DIC and GFP filters
591 controlled by ZEN software (version 2.5). Images were captured using a Hamamatsu C11440 digital
592 camera. For scoring plate level phenotypes, images were acquired using a Moticam CMOS (Motic)
593 camera attached to a Zeiss dissecting microscope.

594

595 Wide-field Fluorescence microscopy:

596 Images were acquired with a Zeiss Axio Observer microscope equipped with Nomarski and
597 fluorescence optics as well as a Hamamatsu Orca Flash 4.0 FL Plus camera. An LED lamp emitting
598 at 470 nm was used for fluorophore excitation. For single images, animals were immobilized on 2%
599 agarose pads supplemented with 100mM Levamisole (Sigma). For single images, animals were
600 immobilized on 2% agarose pads supplemented with 100mM Levamisole (Sigma). For long-term
601 imaging methods, see Microfluidics and Long-term Imaging section.

602

603 **Fluorescent Reporter Quantification.** Reporter lines were imaged using wide-field fluorescence or
604 confocal microscopy as described above. The average intensity (arbitrary unites) per seam cell was
605 measured using ImageJ. Each seam cell intensity was determined by the measurement of fluorescent

606 intensity of the nucleus minus the intensity of a background sample. The fluorescent intensity of each
607 animal was determined by the average of three seam cells. Ten animals per developmental stage
608 were imaged unless otherwise noted.

609

610 **MCP-GFP live imaging**.

611 Long term imaging: For long-term live imaging across several larval stages, animals were mounted
612 in a microfluidic chamber 6h after L1 arrest and grown on NA22 bacteria suspended in S-medium
613 until mid L4 as previously described (*22*). At each time point, animals were *reversibly* immobilized
614 using microfluidic pressures and flows. A z-stack of 51 images separated by 0.5um was acquired at
615 four overlapping positions, covering the entire microfluidic chamber. Thereafter, the animal was
616 released from immobilization and left to roam and feed freely until the next time point.

617

618 Short term imaging: For short-term live imaging (Figs. 1, 4 & 5) developmentally staged animals were
619 mounted into the microfluidic chamber as previously described (*22*), a few hours before the expected
620 appearance of MS2 spots. Minutes before the appearance of MS2 spots, animals were immobilized
621 using microfluidic pressures and flows and kept immobilized for the entire duration of the experiment.
622 This allowed to maintain a stable worm position enabling automated analyses (see below). At each
623 time point (every 4min), a stack of 21 images separated by 0.5um was acquired at four overlapping
624 positions, covering the entire microfluidic chamber. Occasionally, animals arrested development upon
625 prolonged immobilizations, as evident by the cessation of germ line divisions (L2-L4 larvae), the cell-
626 cycle arrest of vulval precursor cells (VCPs) (L3 larvae) or by failure to advance through vulval
627 morphogenesis (L4 larvae). These animals were excluded from further analysis. As opposed to all
628 other genotypes imaged, *nhr-85(0)* mutants animals exhibited a pronounced tendency to roll under
629 these imaging conditions, precluding MS2 spot tracking within nuclei of the lateral hypodermis.

630

631 **MCP-GFP live imaging data analysis.**

632 Short term imaging:

633 All events (cell divisions, onset and offset of MCP-GFP spots) were scored manually in the time
634 series. For short-term live imaging, all analysis was performed using custom-written FIJI macros,
635 pixel classification with random forest trees in Ilastik and MATLAB© scripts. The main challenge in

636 this analysis is residual animal movement between time points as well as low signal-to-noise ratio of
637 the MCP-GFP signal.

638

639 Long term imaging and 3D tracking:

640 First, the worm backbone was detected in each frame by skeletonization, using a thresholded
641 probability map, obtained by processing a maximum z-projection of the MCP-GFP channel, through
642 a custom-trained Ilastik pixel classifier. Next, computational straightening was performed along this
643 backbone (*22*) to obtain a time series of straightened worm z-stacks. This straightened time series
644 has the advantage that residual movement is primarily along the anteroposterior animal axis. Next,
645 we divided the straightened worm z-stack along the worm axis into overlapping (20%) segments of
646 500 pixels (~91um) in length. Each of these segments was then manually registered to obtain z-
647 stacks in which tracking of almost all hypodermal nuclei could automatically performed with minimal
648 user corrections. To improve nuclear signal for segmentation, the histone-mCherry signal was
649 augmented, using a custom-trained Ilastik pixel classifier. 3D tracking and manual correction was
650 then performed on the resulting Ilastik probability maps using the FIJI TrackMate plugin (*53*) with LoG
651 detector and LAP tracker. For each segment, frames with substantial animal movement *between* z-
652 slices were excluded from subsequent analysis. Whenever nuclei were tracked twice (due to
653 overlapping worm segments), the nucleus with the most tracked time points was chosen for
654 subsequent MCP-GFP spot analysis.

655

656 **MCP-GFP spot tracking and intensity quantification.** MS2 spots were tracked in each tracked
657 nucleus, using the FIJI TrackMate plugin with LoG detector and LAP tracker and the Ilastik nucleus
658 probability maps as mask to include only spots inside nuclei. Each MCP-GFP spot track was manually
659 corrected, and spots were added to frames occasionally, in which the TrackMate LoG detector failed
660 to detect them. For quantification of MCP-GFP spot intensities, a 2D Gaussian fit to the maximum z-
661 projection of three z-slices around the peak slice determines the position of the spot. Background
662 was calculated as the average intensity in a ring between 3 and 5 pixels away from the spot position.
663 The spot intensity was calculated by integrating the fluorescence over a circle with a radius of 2 pixels
664 around the spot position and subtracting the estimated background.

665

666 **MS2-MCP-GFP trace analysis.** MCP-GFP traces were smoothed with a Gaussian of width 1.5
667 frames (6 minutes). Using this filtered trace, for each tracked locus, duration and maximum intensity

668 during the transcriptional pulse was determined. Loci were considered “ON”, if spot intensity was
669 above 150 counts and “OFF” if below. Duration of transcription for each locus was determined as the
670 time interval between the first “ON” time point and the last. Typically, loci stayed “ON” for the entire
671 duration of the transcriptional pulse within a given larval stage.

672

673 **Yeast two-hybrid.** Plasmids containing target proteins fused to GAL4 DNA-binding-domain (pDBD)
674 and GAL-4 Activation Domain (pAD) were co-transformed into the pJ69-4a Y2H yeast strain (*54*) as
675 previously described (*55, 56*). Transformed yeast was plated on SC-TRP-LEU plates for three days.
676 Three colonies from each transformation plate were streaked onto SC-HIS-TRP-LEU plates
677 containing 3-AT at the indicted concentrations. Protein interactions were determined by visible growth
678 on 3-AT conditions with negative growth in empty vector controls after three days. For the large-scale
679 LIN-42 screen, pDBD containing LIN-42a, LIN-42b, and the empty vector control were individually
680 mated to each pAD construct from the WTF2.2 yeast library (Reece-Hoyes et al., 2011) (*57*). For
681 visualization of results, individual colonies were grown overnight in YPD in 96-well plates. Overnight
682 cultures were diluted 1/200 in ddH20 and 3µL was pipetted on to selective 3-AT and control plates.
683 After three days of growth, plates were imaged on a Fotodyne FOTO/Analyst Investigator/FX
684 darkroom imaging station. Plasmids used in 1- and 2-hybrid experiments are outlined in Table S4.

685

686 **Bioinformatic analysis of BLMP-1, NHR-82, and NHR-23 ChIP-seq data.** ChIP-seq short reads
687 were first clipped off adaptor sequences. Reads of minimum 22bp were mapped to the UCSC *C.*
688 *elegans* genome (ce10) using bowtie program76 (*58*) looking for unique alignments with no more
689 than 2 mismatches. MACS program (v1.4)(*59*) was used for peak calling with significant p-value cutoff
690 equals 1e-5. Target annotations were based on WormBase (version 220) using customized R scripts
691 and Bioconductor packages. ModeEncode data sets (*48*) (BLMP-1(ENCFF108AEB and
692 ENCFF615AMZ), NHR-23(ENCFF019QMH) and NHR-85(ENCFF018KHA)) were used in the initial
693 analysis and we defined the promoter region as upstream 3kbp to downstream 300bp around the
694 transcription start site (TSS). Peaks located in promoter regions were annotated to their closest TSS
695 sites for both coding and non-coding genes (Table S1). These potential targets were then overlapped
696 to sets of oscillatory genes identified in a previous mRNA-seq-based study (*8*). Overlapping target
697 gene sets organized in Figure 2D are from postembryonic ChIP-seq samples for each TF. Raw data
698 for each of the 265 ModEncode data sets (annotation numbers listed individually in Table S1) used
699 in Figure 2E were downloaded from modENCODE (*48*) and processed in the same way as BLMP-1,
700 NHR-23 and NHR-85 datasets (*11*). ModEncode-derived peaks from each TF ChIP-seq dataset were

701 compared to identify common sites with at least one base pair overlapping using BEDTools. All ChIP-
702 seq mapping graphs and images were produced in R by customized scripts.

703

704 **Protein preparation.** Full-length *C. elegans* protein NHR-23 was cloned as a N-terminal Strep-
705 SUMO fusion protein in a pFL vector of the MultiBac Baculovirus expression system to create
706 pCMH1662 (*60*). This construct was expressed in insect *Sf9* cells grown in CCM3 media (HyClone)
707 at 27°C for 60 h. Cells were harvested by spinning at 2200 rpm for 20 min and resuspended in
708 lysis/wash buffer (20 mM Tris pH 8.0, 200 mM NaCl, 5 mM BME) and a protease inhibitor cocktail
709 before flash freezing in liquid N_2. Cell pellets were stored at -80°C. Cell pellets were thawed and
710 sonicated once. Poly-ethylene imine (PEI) was added at 0.2% to the lysate after cell pellets were
711 thawed and sonicated. The lysate was then spun by ultracentrifuge at 38,000 rpm for 45 min, at 4°C.
712 The supernatant of the lysate was then used for batch binding with Strep-Tactin superflow resin (IBA)
713 for 1 hour while on a rolling shaker at 4°C. The affinity beads were harvested by spinning at 1000 rcf
714 for 5 minutes, then resuspended in lysis/wash buffer and applied to a gravity column. The column
715 was washed with 30 column volumes of lysis/wash buffer and 5 column volumes of ATP wash buffer
716 (20 mM Tris pH 8.0, 200 mM NaCl, 5 mM BME, 2 mM ATP). The protein was eluted from the affinity
717 column in 2 column volumes of elution buffer (20 mM Tris pH 8.0, 200 mM NaCl, 5 mM BME, 2 mM
718 desthiobiotin). The Strep-SUMO tag was cleaved from NHR23 by ULP1* protease overnight at 4°C.
719 The protein was then concentrated and loaded onto a 10/300 Superdex200 Increase gel filtration
720 column (Cytiva Life Sciences), running in lysis/wash buffer, chromatographed for ~30 mL at 0.6 mL
721 min^{-1}. Protein purity and cleavage efficiency was assessed by SDS-PAGE. Plasmids used to express
722 recombinant proteins are outlined in Table S4.

723

724 Full length *C. elegans* protein NHR-85 was cloned as a N-terminal Strep-fusion protein in a pFL vector
725 of the MultiBac Baculovirus expression system to create pCMH2206. NHR-85 was purified using the
726 same method as above, with the exception of the overnight N-terminal tag cleavage step.

727

728 **Microscale thermophoresis analysis.** Binding assays of purified NHR23 or strep-NHR85 was
729 measured using a Monolith NT.115 Pico running MO Control version 1.6 (NanoTemper
730 Technologies). Assays were performed in 100 mM NaCl, 20 mM Tris pH 8.0, 0.05% Tween-20.
731 AlexaFluor647 NHS Ester (ThermoFisher Scientific) labeled NHR-23 (200 pM) was mixed with 16
732 serial dilutions of strep-NHR-85 starting at 31.5 uM and loaded into microscale thermophoresis

733 premium coated capillaries (NanoTemper Technologies). MST measurements were recorded at 25°C
734 using 30% excitation power and 60% MST power. Measurements were performed in duplicate.
735 Determination of the binding constant was performed using MO Affinity Analysis v.2.3.

736

737 AlexaFluor647 NHS Ester (ThermoFisher Scientific) labeled strep-NHR-85 (400 pM) was mixed with
738 16 serial dilutions of NHR-23 starting at 625 nM. MST measurements were recorded at 25°C using
739 15% excitation power and 40% MST power. Measurements were performed in triplicate.
740 Determination of the binding constant was performed using MO Affinity Analysis v.2.3.

741 **Gel Shifts.** For gel shifts with free DNA, 5' IRDye (IRDye700 or IRDye800)-labeled and unlabeled
742 oligos were obtained from IDT (Coralville, Iowa) and used to amplify DNA probes of the indicated
743 sequences. For wild-type probes, the indicated PCE fragments were amplified pCMH1954. For
744 mutants probes that harbor mutations in either of the GGTCA repeats, synthetic DNAs were obtained
745 from Synbio Technologies (Manmouth Junction, NJ, USA) and used to amplify the corresponding
746 mutant DNA fragments with the following sequences (mutations underlined and italicized):

747 C_ROR(1)REV:TTTGCATCCTCATTCTCAACACCTCGTTTTTTTCCCTTTTCTTGCACAAATTGA*cc*
748 *tgt*GTCGGTCAGTAAACCCCCCCCCCCCCCCCCCCCATTGAGGTGACCAATTGGTTTTTCTTTTCC
749 TTTACTTTCTCCTTCACTTTCTCTCTC TCGGATCACCAGC

750 C_REV:TTTGCATCCTCATTCTCAACACCTCGTTTTTTTCCCTTTTCTTGCACAAATTGAGGTCAG
751 TC*cctgtc*TAAACCCCCCCCCCCCCCCCCCCCATTGAGGTGACCAATTGGTTTTTCTTTTCCTTTAC
752 TTTCTCCTTCACTTTCTCTCTC TCGGATCACCAGC

753 For binding reactions, recombinant proteins were incubated with gel purified DNA probes in 10 mM
754 Tris pH 7.5, 50 mM KCl, 1 mM DTT, 0.1mg/mL poly (dIdC) (Sigma-Aldrich), and 0.25% Tween 20
755 for 30 minutes at 20°C (in dark chamber). Samples were then run in a 4% native polyacrylamide gel
756 containing 50mM Tris pH 7.5, 0.38 M glycine and 2mM EDTA in 1x TBE buffer. Gels were imaged
757 and quantified using a Li-Cor Odyssey Imager (Lincoln, Nebraska).

758

759 **Graph Plots and Statistical Analysis.** Plots and diagrams were generated using GraphPad Prism
760 v9 (GraphPad Software, San Diego, Ca) or custom-written MATLAB® scripts. Statistical significance
761 was determined using a two-tailed un-paired Student's t-test. $P<0.05$ was considered statistically
762 significant. **** indicates $P < 0.0001$.

763

764 Table S1. Annotation of ChiP-seq Data from ModEncode used in Fig. S3.

765 Table S2. Table depicting the distribution of ChIP-seq target genes for each TF parsed out into
766 expression categories outlined in Fig. S3.

767 Table S3. *C. elegans* and yeast strains used this work.

768 Table S4. List of plasmids used in this work.

769

770 **BIBLIOGRAPHY:**

771 1. G.-J. Hendriks *et al.*, *Mol Cell* **53**, 380-392 (2014).
772 2. C. L. Araya *et al.*, *Nature* **512**, 400-405 (2014).
773 3. S. Brenner, *Genetics* **77**, 71-94 (1974).
774 4. A. G. Fraser *et al.*, *Nature* **408**, 325-330. (2000).
775 5. R. S. Kamath *et al.*, *Nature* **421**, 231-237 (2003).
776 6. D. J. Dickinson *et al.*, *Nature methods* **10**, 1028-1034 (2013).
777 7. J. E. Sulston, H. R. Horvitz, *Developmental biology* **56**, 110-156. (1977).
778 8. W. Keil *et al.*, *Developmental cell*, (2016).
779 9. D. Ershov *et al.*, *Nat Methods* **19**, 829-832 (2022).
780 10. P. James *et al.*, *Genetics* **144**, 1425-1436 (1996).
781 11. A. J. Walhout *et al.*, *Yeast* **17**, 88-94 (2000).
782 12. A. J. Walhout, M. Vidal, *Methods* **24**, 297-306 (2001).
783 13. J. S. Reece-Hoyes *et al.*, *Nat Methods* **8**, 1059-1064 (2011).
784 14. K. L. Borden, *Biochemistry and cell biology = Biochimie et biologie cellulaire* **76**, 351-358
785 (1998).
786 15. Y. Zhang *et al.*, *Genome biology* **9**, R137-139 (2008).
787 16. N. Stec *et al.*, *Curr Biol* **31**, 809-826 e806 (2021).
788 17. C. Bieniossek *et al.*, *Current protocols in protein science* **Chapter 5**, Unit 5.20-25.20.26
789 (2008).

790

791